Università degli Studi di Milano

Faculty of Medicine and Surgery
Specialization School in Medical Physics

Evaluation of the proton range accuracy using Single and Dual Energy Computed Tomography

Advisor:
Prof. Cristina Lenardi

Co-Advisors:
Dr. Federica Cattani
Dr. Floriana Pansini

Outside Examiners:
Dr. Juan Antonio Vera Sánchez
Dr. Nicoletta Paruccini

Candidate:
Davide Alio
ID Number S65864

Academic Year 2022/2023

Summary

Proton therapy is a highly advanced form of external beam radiotherapy, which uses proton beams to treat cancers. Protons are particularly suited for radiotherapy because heavy particles, interacting with matter, deposit most of their energy at the end of their track. It allows for well-conformed dose distributions to the target area while minimizing exposure to surrounding healthy tissues and organs at risk. In addition, ongoing research reveals that protons have distinct biological, immunological, and clinical effects compared to photons, beyond just dose distribution differences.

X-ray CT images are currently the standard for proton beam planning, but they have limitations due to the need to convert electron density maps into stopping power ratios (SPR) maps. CT numbers (HU values) noise and the lack of a consistent conversion to SPR lead to imperfect dose calculations and introduce density uncertainties. Additionally, CT scans only capture a single snapshot of patient anatomy, while daily variations during treatment cause setup uncertainties. Treatment planning systems (TPSs) are designed for account density and setup uncertainties through robust optimization. Density and setup uncertainty values are not uniquely defined. They are institution-specific, depending on the utilized treatment modalities, the clinical experience and the target anatomic localization. Density uncertainty typically ranges within 3% and 3.5%, whereas, setup uncertainty varies from 1 mm up to 5mm.

Within the scientific community, there is a strong interest in reducing the density uncertainties. The advent of Dual-Energy CT (DECT) scanners has introduced new options to increase the SPR conversion accuracy compared to Single-Energy CT (SECT). The Siemens Syngo.via software is an available commercial solution to perform the DE raw image processing, generating Dual Energy Monoenergetic Plus images. In addition, the software includes a tool, DirectSPR, able to directly calculate voxel by voxel the proton SPR, without resorting to HU conversion.

This work aims to evaluate the impact of HU to SPR conversion methods on TPS proton range estimation. HU to SPR conversion relationships were derived from CT calibrations. The following methods were implemented and evaluated: the SECT tissue-substitute method and, on the other hand, the SECT and Dual Energy Monoenergetic Plus Stoichiometric calibration

methods. In different scenarios, the proton range was directly measured with a multi-layer ion chamber and compared with the one derived from TPS dose calculation on DirectSPR maps and SECT and DECT images.
Firstly, tissue-surrogate solid plugs were individually irradiated with a single pencil beam of 226 MeV proton. DirectSPR-derived proton range showed a better agreement with measurements than CT calibration-based methods differing at most by 1% (SECT and 75KeV Monoenergetic Plus with the stoichiometric calibration respectively by 6.5% and 4.5%), for all the plugs except for high-density ones. All the TPS calculated proton ranges significantly differed (up to 32%) from the measurement for the He Cortical Bone plug. This result will require additional investigation.
Plug results can not be fully translated to human tissues, since they have different chemical compositions. For this purpose, animal organ samples were used. They were irradiated with single pencil beams of different energies (100 MeV, 150 MeV and 226 MeV) and with a simple intensity modulated proton therapy (IMPT) plan (a dose cube). Three irradiation points were identified on each sample surface and the proton range was probed at each of them. Proton range differences between measures and TPS-derived ones had no dependency on beam energy. However, the results of this investigation do not confirm the high accuracy in SPR assignment of DirectSPR than SECT and DECT calibration-based methods, indeed, proton range differences with measures were very close within the various approaches.

The density uncertainty was evaluated on the data derived from IMPT irradiation on animal organ samples, given the closeness to clinical treatment conditions. A value of 2% could be taken as density uncertainty associated with the use of SECT and Monoenergetic Plus 75keV image with the relative stoichiometric calibration curve in proton dose calculation, while the value obtained for the DirectSPR was higher, 2.8%. The high standard deviations of the multiple irradiation point measurements suggest the presence of residual setup errors affecting the results and the necessity to improve setup repeatability for further investigations.

The results of this study confirm the feasibility of the use of DirectSPR and Monoenergetic Plus images generated by the Syngo.via software as input to the Raystation TPS for proton dose calculation. Although preliminary, the results of this study support the reduction of the 3.5% clinical density uncertainty enabled by the implementation of dual-energy CT as suggested by many authors.

Contents

List of Figures

List of Tables

Chapter 1

Introduction

Over the last decades, proton therapy has become a more widely available treatment modality. Chordomas, chondrosarcomas, sarcomas, intracranial meningiomas, ocular tumours, pediatric solid tumours and retreatments are among the pathologies for which proton therapy is indicated in Italy according to ministerial LEA (essential levels of assistance). Heavy particles interact with matter depositing most of their energy at the end of their track and their penetration depth is controllable by varying their initial energy. This interaction mechanism is ideal for radiotherapy, especially for critical diseases such as the ones cited above, guaranteeing similar dose coverage to the target region than photon IMRT (intensity modulated radiotherapy) techniques, but reducing the integral dose [1].

While dose calculation algorithms are always more accurate and delivery systems are always more precise, proton range uncertainty remains an open issue [2]. Robust planning allows accounting for it, resulting in larger margins and irradiation of healthy tissue.
The range uncertainty is mainly due to density uncertainties. The density uncertainty originates from the non-unique conversion relationship between CT numbers, the Hounsfield Units (HU), and the material composition required by the Monte Carlo engine for dose calculation. CT calibration procedures define the conversion relationship between HU and mass density or stopping power ratios (SPR) and treatment planning systems (TPSs) assign the material composition based on it. The uncertainty associated with the conversion and the intrinsic CT image noise results is a total density uncertainty of 3-3.5%.

Dual-Energy CT (DECT) scanners, acquiring two images using different spectral distributions have the potential to obtain more information on the composition of materials within each voxel [3]. The processing of the two acquired images produces Virtual Monoenergetic Images (VMI) and SPR maps which are valid alternatives to the Single-Energy CT image as the basis for dose calculation. The Syngo.via Software (Siemens Healthineers, Erlangen, Germany) is an available commercial solution to perform the raw image processing, generating Dual Energy Monoenergetic Plus images and DirectSPR maps.

Multiple previous studies [4–7] examined the feasibility of using SPR data generated from DECT for treatment planning, demonstrating its higher accuracy in SPR assignment than SECT calibration methods. Instead, the purpose of this study was to investigate the impact directly on the proton range. Tissue-surrogate plugs and animal organ samples were irradiated to compare the measured proton range, in terms of the distal 90% range ($D_{90\%}R$, with the one calculated by the Treatment Planning System. Specifically, the dose was computed using DirectSPR maps, SECT images, and Dual Energy Monoenergetic Plus images. The following CT calibration methods were implemented and evaluated: on the one side SECT tissue-substitute method, on the other side SECT and Dual Energy Monoenergetic Plus Stoichiometric calibration [8].

Chapter 2

Proton Therapy

Proton therapy is one of the most advanced forms of external beam radiotherapy, which uses proton beams to irradiate diseased tissue, most often to treat cancer. Over the last two decades, there has been an explosive growth in proton centres around the world. According to Particle Therapy Co-Operative Group (PTCOG)[9], 136 hadron therapy facilities, of which 121 are equipped with proton beams, are in clinical operation worldwide, 31 are under construction and 35 are in the planning stage.

2.1 Physical and biological principles

Originally, the central rationale for proton therapy was its spatial dose distribution tightly conformed to the tumour target. In recent years, advances in photon therapies, such as intensity-modulated photon therapy and volumetric modulated arc therapy have diminished the advantage of protons over photons in this aspect. However, the containment of low doses and the "dose bath" avoidance allow protons to spare normal tissue more effectively than photons. Moreover, ongoing research is leading to the realization that protons are very different from photons in terms of their complex biological, immunomodulatory and clinical effects beyond just the differences in dose distributions.
The principal interaction mechanisms of protons (in the clinical range of 70 to 230 MeV) with matter are Coulomb interactions with atomic electrons, Coulomb interactions with nuclei, and nuclear interactions [10]. To a first-order approximation, protons continuously lose kinetic energy interacting with atomic electrons via inelastic Coulomb scattering. Most protons travel in a nearly straight line because the proton mass is 1832 times greater than that of an electron. Deflection from its original straight-line trajectory is the result of the elastic Coulomb scattering of a proton experiencing the repulsive electric field of a nucleus. Inelastic nuclear reactions between protons and the atomic nucleus have a smaller cross-section with respect to the other two interaction mechanisms; in a nuclear reaction, the projectile proton enters the nucleus causing the emission of proton, deuteron, triton, heavier ions and/or some neutrons.

The energy loss rate of particles, or linear stopping power (S) is defined as the quotient of dE and dx, where E is the particle energy and x is the distance in a material. The mass stopping power is the energy loss rate divided by the mass density (ρ). The linear stopping power for a particle beam is accurately described by the Bethe and Bloch theory summarised in the formula (Eq.2.1:

$$\frac{S}{\rho} = -\frac{dE}{\rho dx} = 4\pi N_A r_e^2 m_e c^2 \frac{Z}{A}\frac{z^2}{\beta^2}\left[ln\left(\frac{2m_e c^2\gamma^2\beta^2}{I}\right) - \beta^2 - \frac{\delta}{2} - \frac{C}{Z}\right] \tag{2.1}$$

where N_A is Avogadro's number, r_e is the classical electron radius, r_e is the mass of an electron, z is the charge of the particles, Z is the atomic number of the absorbing material, A is the atomic weight of the absorbing material, c is speed of light, β = v/c where v is the velocity of the particles, $\gamma = (1-\beta^2) - 1/2$, I is the mean excitation energy of the absorbing material, δ is the density correction item arising from the shielding of remote electrons by close electrons and will result in a reduction of energy loss for higher energies, and C is the shell correction item.
This process of energy deposition produces the characteristic depth-dose curve, the Bragg curve, for a monoenergetic beam of protons as illustrated in Fig. 2.1. Proton beams enter and travel through water or tissues with lower dose deposition at the entrance and along their path, depositing the greatest part of the dose just before stopping, where a peak, the Bragg peak, occurs. Instead, beyond the Bragg peak, the dose falls rapidly and sharply to zero. By comparison, photons deposit their peak dose at build-up, close to their entrance into the tissue, and thereafter, there is an exponential decrease of deposited dose with increasing depth. The Bragg peak width of a monoenergetic proton beam is typically inadequate to fully cover the treatment target, thus multiple monoenergetic narrow beams of appropriate energy are employed to create a "spread-out Bragg peak" (SOBP).

The Relative Biological Effectiveness, RBE, is defined as the ratio of the dose of a reference radiation (photons) to the dose of a test radiation that is required to produce the same biological effect. In proton therapy a constant RBE of 1.1 is standardly used, as recommended by the International Commission on Radiation Units [12]. The Linear Energy Transfer, LET, is the energy loss and deposition along the path of a proton beam. It is a measure of ionization density. Under $100 keV/\mu m$ RBE and LET are strongly correlated. Indeed, higher LET particles produce denser ionization events, resulting in more extensive damage induction. High-energy proton beams are considered low-LET irradiation. Slowing down interacting with matter, their LET increases particularly at the distal edge. Consequently, RBE values have been reported to rise from 1.1 in the entrance, to 1.2 in the centre, 1.4 at the distal edge, and 1.7 to 2.5 or 3.5 in the distal fall-off the SOBP [2, 13]. This increase in RBE is still a subject of discussion and the clinical impact is under study.

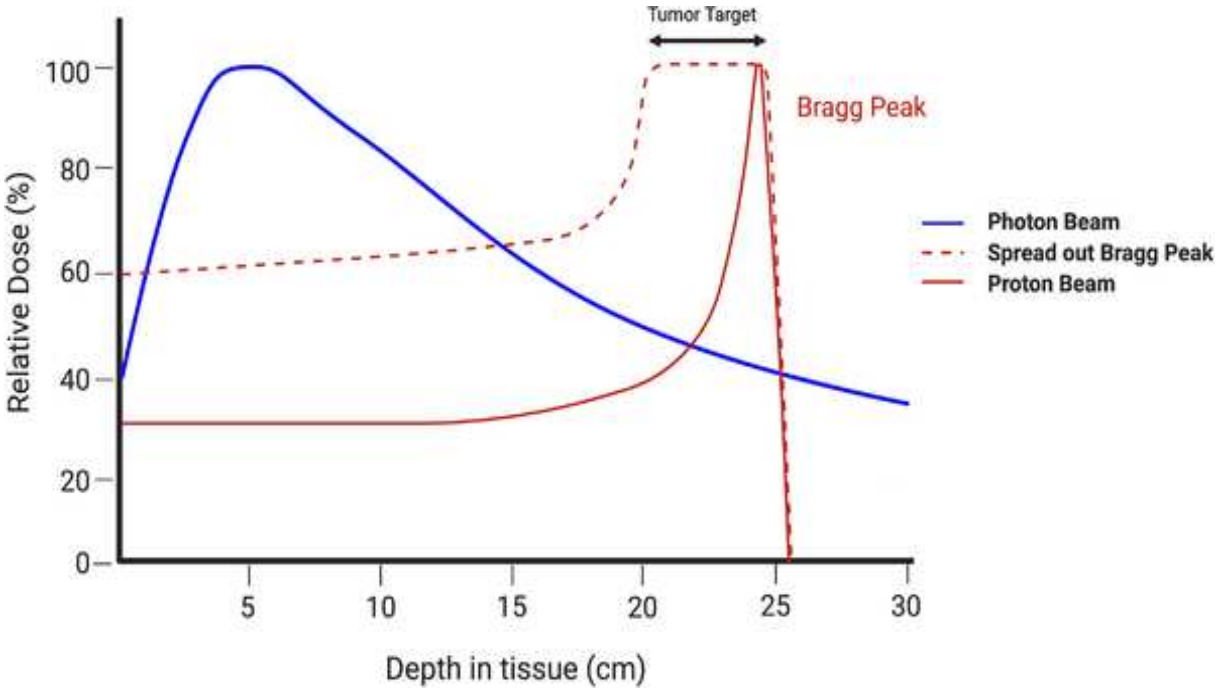

Figure 2.1: Comparison of relative depth dose distributions of photons versus protons.[11]

2.2 Proton Therapy Delivery Mechanisms and Systems

For therapeutic purposes, protons are typically accelerated to energies within 70 and 230 MeV, corresponding to proton ranges in water within 4 and 32 cm, through cyclotrons, synchrotrons and synchrocyclotrons. Cyclotrons are more compact than synchrotrons and produce a continuous stream of protons, accelerating them to the machine's maximum energy; lower energy beams are achieved by inserting an energy degrader in the path of protons. Synchrocyclotrons are a special type of cyclotron, in which the frequency of the driving RF electric field (constant in classical cyclotrons) is varied to compensate for relativistic effects. A pulsed beam with a frequency of 1 kHz is yielded. Synchrotrons, in contrast, directly accelerate proton batches to the desired energy, resulting in less intensity loss. In all accelerators, proton beams are guided through the beamline into the treatment room, and the nozzle is eventually mounted on a rotating gantry. The nozzle can be equipped with a range shifter that allows for positioning the Bragg peak at a depth of a few millimetres inside the patient's body. It is used to treat superficial targets and modulate the dose up to the skin surface. Modern techniques employ scanning beamlets of protons to achieve dose distributions that conform to the shape of the target volume and optimally spare normal tissues. For each beam, the treatment is delivered in layers, one per energy. Contributions from multiple beams produce the desired pattern of dose. Scanning magnets, placed before the nozzle, allow precise direct beamlets and the delivery of intensity-modulated proton therapy (IMPT). For IMPT, the energies of beamlets are defined based on the positions of spots (Bragg peak of each beamlet) within the target volume. The intensities of beamlets are determined using inverse planning optimization techniques to achieve the closest approximation of the desired dose distribution.

2.3 Proton Therapy Treatment planning

The first dose calculation models for proton treatment planning employed raytracing methods, which only considered the deposition of dose along straight lines from the source to the point of interest in the patient's body. Increased computing power has allowed us to overcome the limitations of these algorithms, leading to the adoption of the analytical pencil beam (APB) model. The APB dose engine divides the beam into many closely spaced mini-beams, known as pencil beams. Each pencil beam dose is calculated by factoring in the lateral proton fluence and the integrated depth dose along its central axis. The lateral proton fluence for each pencil beam is influenced by stopping power, Multiple Coulomb Scattering, and nonelastic nuclear scattering. The total dose distribution is obtained by summing the contributions from all individual pencil beams. However, the presence of lateral heterogeneity, particularly in lung targets, caused inaccuracies in dose calculations.
RaySearch Laboratories introduced a Monte Carlo (MC) dose calculation engine in May 2017 to replace the APB algorithm in the RayStation treatment planning system (TPS). This development significantly improved the accuracy of proton beam dose calculations within patients. Notable improvements were observed in dose calculations for targets in the lungs and inhomogeneous mediums, when using an aperture to sharpen the beam edge or in the presence of a range shifter with large air gaps [14].
Two different techniques are available: single-field optimized (SFO) and multifield optimized (MFO). In SFO, the intensities of beamlets for each beam are optimized individually without considering other beams, aiming to produce uniform dose distribution within the target volume and minimize the dose outside it. In MFO, all beams are optimized simultaneously to balance the dose and dose-volume objectives for normal tissues and target volumes, providing greater flexibility to achieve optimal dose distribution patterns, especially for complex anatomical geometries.
In addition to uncertainties stemming from the physical model implemented in the MC dose calculation algorithm, other sources of uncertainty have to be evaluated and accounted for in proton therapy planning.
TPSs calculate proton therapy doses based on a three-dimensional map of relative proton-stopping powers (compared to water) of the anatomical structures traversed by the beams. Proton CT images [15] are a promising new imaging technique that can directly reconstruct relative stopping power maps with high accuracy. Technical development is ongoing, and commercial scanners are expected to be available in the next few years. Currently, X-ray CT images are standard for proton beam treatment planning, but they have several limitations. Electron density maps are extracted from these images, but they have to be converted into relative stopping power maps. Systematic uncertainties in these conversions are inevitable due to the differences in the physics of X-ray and proton interactions with matter. This topic will be explored in greater detail in the next chapter (Chap. 3). In addition, the proton range accuracy is degraded also by the intrinsic CT image noise.

Moreover, the planning CT provides only a snapshot of possible patient geometry, while daily variations may occur during treatment. Careful patient preparation, positioning, and daily online Image-Guided Radiation Therapy (IGRT) help reduce setup uncertainty. While rigid inter-fraction shifts can be prevented, non-rigid inter-fraction motions, intra-fraction tumour volume variations, and organ motion are significant sources of uncertainty. Setup uncertainties are not unique to proton therapy; photon therapy is also affected, though the impact is more important in proton therapy due to the physics heavy particles. Photons are more "robust" than protons; small variations in the density, composition, or width of the tissue they traverse result in limited dose variations along their path. In contrast, without robust optimization, such variations would directly affect the Bragg Peak position of proton beamlets, causing high doses to be deposited outside the target area, leading to under-coverage of the target and higher irradiation of organs at risk (OAR).

In photon therapy, setup uncertainties are taken into account through the expansion of the clinical target volume (CTV) into the planned target volume (PTV) and prescribing the dose to it. Margins are defined by van Herk's formula [16], based on the request that 95% of CTV has to be covered by the 95% of the prescribed dose. Albertini et al. [17] highlighted the ineffectiveness of this approach for proton therapy. They evaluated the robustness of IMPT plans, optimized by prescribing to the PTV, concerning density and patient position uncertainties. Particularly for IMPT high-gradient plans, significant dose uncertainties were found, even in the centre of the target volume. The use of a PTV did not enhance the robustness of the plan, neither in the CTV region.

The first step to plan robustly is a proper choice of beam direction. The impact of range uncertainties is reducible by increasing the number of beam directions. In addition, selecting beam directions not to go through regions subjected to significative anatomical or density variation results in more robust plans.

Currently, TPSs, such as RayStation, are designed for robust optimization. In RayStation, the min-max optimization method is implemented. This algorithm simultaneously considers all selected robust optimization functions, evaluating each across different scenarios. The worst-case scenario is the scenario in which the optimization function weighted sum attains its highest value. Feasible variables (e.g. spot positions) are varied to minimize this sum. The formalism is summed up in the following equation (Eq.2.2):

$$\min_{x \in X} \max_{s \in S} \sum_{i=1}^{N} w_i f_i(d(x;s)) \tag{2.2}$$

where X is the set of feasible variables, S is the set of scenarios, f_i is the i-th optimization function asked to be robust of weight w_i that depends on the dose distribution as a function of the variable x and the scenario s. Possible scenarios are defined assuming systematic density uncertainty and systematic or interfraction (random) patient setup errors or a combination of both. In addition, variability given by organ motion, e.g. breathing, can be included in the evaluated scenario assuming systematic shifts, random shifts or performing the optimization on the various phases of 4DCT acquisition.

Density and setup uncertainty values are not uniquely defined. They are institution-specific, depending on the utilized treatment modalities, the performance of the equipment, the choice of dose calculation engine, the clinical experience and the target anatomic localization. Density uncertainty typically ranges within 3% and 3.5% [18], whereas, more variability characterizes setup uncertainty varying from 1 mm up to 5mm.

Chapter 3

CT HU numbers to Stopping Power Ratio Conversion

The primary source of inaccuracy in proton dose calculation stems from the precise determination of proton range. TPS dose calculations rely on a three-dimensional map of proton SPR across anatomical structures traversed by the beams, derived from X-ray CT images. However, CT numbers (HU values) suffer from the lack a consistent conversion relationship to proton SPR, making them imperfect inputs for dose calculations.
CT calibrations define either direct or indirect curves converting HU to SPR. Indirect calibration involves first converting HU values to mass densities. For Monte Carlo dose engines, for each CT voxel, its material composition must be fully described in term of mass density, mass fraction of atomic elements, and mean ionization energy (I). A list of template materials with known chemical compositions and physical properties is defined in the TPS. The mass density assigned to a voxel from the HU conversion is used for obtaining the elemental composition and mean ionization energy calculation, attributing the ones of template materials with the closest mass density. In contrast, direct conversion assigns the template material (and its properties) closest to the voxel's SPR. In both cases, the material composition of the voxel is inputted to calculate the SPR taking into account the energy of each proton beam.
The most common calibration methods are the tissue-substitute method and the stoichiometric method [8]. The tissue-substitute method creates a calibration curve by scanning materials with known mass densities that mimic human tissues and correlating these densities with measured CT numbers through linear interpolation. Details on the stoichiometric method are discussed in Section 3.1. The advent of Dual-Energy CT (DECT) scanners has introduced new options aimed at reducing the inaccuracies associated with Single-Energy CT (SECT). This work aims to evaluate the impact of using Virtual Monoenergetic Images (VMI) and SPR maps derived from Dual Energy acquisitions on density uncertainty.

3.1 Stoichiometric Calibration

The attenuation of a photon beam for energies up to 1 MV is led by photoelectric absorption and coherent and incoherent scattering. The relation can be written in the form [19, 20]:

$$\mu = \rho(\sigma^{ph} + \sigma^{coh} + \sigma^{incoh}), \tag{3.1}$$

where μ is the linear attenuation coefficient of the material, ρ is its electron density and σ^{ph}, σ^{coh} and σ^{incoh} are the cross-sections for the photoelectric effect, coherent scattering and incoherent scattering respectively. The HU numbers from a CT image are derived from the linear attenuation coefficient, following the relation:

$$\mu_r = \frac{\mu}{\mu_w} = \frac{HU + 1000}{1000}, \tag{3.2}$$

where μ is the linear attenuation coefficient of the material, μ_w is the one of the water. Using the parametrization introduced by Rutherford and al. [21] the equation 3.1 can be written as follow:

$$\mu = \rho \left(K^{ph}\, \tilde{Z}^{3.62} + K^{coh}\, \hat{Z}^{1.86} + K^{NN} \right), \tag{3.3}$$

with

$$\tilde{Z} = \left[\sum_i \lambda_i\, Z_i^{3.62} \right]^{1/3.62}, \tag{3.4}$$

$$\hat{Z} = \left[\sum_i \lambda_i\, Z_i^{1.86} \right]^{1/1.86}, \tag{3.5}$$

and

$$\lambda_i = \frac{\frac{\omega_i\, Z_i}{A_i}}{\sum_i \frac{\omega_i\, Z_i}{A_i}}. \tag{3.6}$$

K^{ph} and K^{coh} are constants which characterize the different cross-sections and K^{NN} is the Klein–Nishina cross section. The three constants depend mainly on the CT device and the acquisition settings. ω_i, Z_i and A_i are respectively the mass fraction, atomic number and mass number of element i in the mixture of which a material is composed.

The rationale of the stoichiometric calibration is to train a linear regression model on images of materials with known electron density, mass density and elemental composition and then apply it to the tissue dataset listed in the ICRP 23 [22]; the dataset contains the same details for 35 human tissues. The linear interpolation of the calculated HU of these 35 tissue to their mass density is the calibration curve. Ainsley and Yeager [23] advice implementing the regression fit procedure reducing the number of the free parameters in the fit constraining HU = 1000 and $\rho_r = 1$ for water and weighting the measured HU on their SD. The resulting equation is:

$$HU + 1000\,(1 - \rho_r) = A \left[\rho_r \left(\tilde{Z}^{3.62} - \tilde{Z}^{3.62}_{water} \right) \right] + B \left[\rho_r \left(\hat{Z}^{1.86} - \hat{Z}^{1.86}_{water} \right) \right], \tag{3.7}$$

HU is the material average HU value measured on its CT image; ρ_r, $\tilde{Z}^{3.62}$, $\tilde{Z}_{water}$, $\hat{Z}^{3.62} and \hat{Z}_{water}$ are determined from its known chemical and physical properties; A and B are the free parameters of the linear regression fit.

3.2 Dual Energy CT principles and Virtual Monoenergetic Images

While SECT images are obtained by a spiral scan with fixed tube tension, typically 120 kVp for planning purposes, DECT acquisitions require two spiral scans at different tube kVp, usually 80 kVp and 140 kVp. Information from each image is combined, resulting in an image with superior tissue differentiation than SECT. Different acquisition technologies have been developed and implemented in clinics [24, 25]. One approach involves the use of two separate imaging chains, each equipped with its own source and detector. Images are reconstructed from simultaneous scans, allowing for relatively close spatial alignment. The tube voltage can be adjusted to maximize spectral contrast and radiation dose efficiency. However, a limitation of this technology is the small usable field of view (FOV) due to the detector size, which is constrained by the CT gantry dimensions. Additionally, cross-scatter between the two source-detector combinations may introduce bias and noise.
Alternatively, DECT can be performed using a single X-ray source capable of rapidly switching between two energy levels, combined with a detector that has a very fast readout capability. This method offers excellent temporal resolution, with minimal delay between low- and high-energy projections (<0.5 ms), cost-efficiency, and a 50 cm FOV. Furthermore, spectral deep learning reconstruction has been developed for this technology, significantly reducing image noise. However, limitations in current modulation during energy switching can reduce the signal from the low-energy spectrum and increase the output from the high-energy spectrum.
A third solution uses a single detector equipped with two distinct scintillator layers to separately capture high- and low-energy data sets. These scanners offer excellent temporal resolution, with no delay between the two energy acquisitions, and also provide exceptional spatial resolution. A large 50 cm FOV does not limit the gantry's rotation speed. However, the detector struggles to sharply discriminate between lower- and higher-energy photons due to overlapping sensitivity profiles of the two layers. This issue is mitigated by an interlayer filter, though at the cost of dose efficiency.
A fourth solution utilizes a single source and detector with a split filter, made of gold and tin, at the X-ray tube, which filters the low- and high-energy beams, respectively. The spectrum is divided into two overlapping halves, each acquired by the corresponding halves of the detector. Dose reduction techniques can be applied, allowing for an exposure dose comparable to single-energy CT (SECT). The low-complexity hardware also enables this technology to be integrated as an upgrade to some SECT scanner models. However, disadvantages include possible cross-scatter between the beams, spectral overlap in the central 2–3 mm of the beam,

and spectral mixing at the detector edges due to penumbra effects. Additionally, the pitch value is limited to 0.5, resulting in longer scan times.
Another solution involves two successive acquisitions using a single X-ray tube and detector array, with fast kVp switching between scans. The main advantage of this approach is that it requires no significant hardware modifications to the SECT scanner, and dose-reduction techniques are available. However, the time delay between high- and low-energy acquisitions can introduce temporal misregistration and patient motion, potentially distorting the spectral data.
The mathematics theory behind DECT was developed by Alvared et al. [26] in 1976. Today technology is mature and efficient. Commercial scanners are available and multi-slice detector array makes acquisitions duration within a few tens of seconds. Even the radiation dose due to the two scans is not significantly higher than the SECT one [27, 28].
Below, DECT principles are described. Please refer to the Report of AAPM Task Group291 [20] for more details about principles and applications of multi-energy CT.
Denoting the mass attenuation functions due to the photoelectric effect and Compton scattering respectively by $f_p(E)$ and $f_c(E)$, the total mass attenuation coefficient can be defined as:

$$\left(\frac{\mu}{\rho}\right)(E) = \alpha_p f_p(E) + \alpha_c f_c(E), \tag{3.8}$$

where α_p and α_c are the $\left(\frac{\mu}{\rho}\right)_{Photoelectric}$ and $\left(\frac{\mu}{\rho}\right)_{Compton}$ contribution to the total attenuation; they are energy-independent. Ignoring the K-edge, $f_p(E)$ and $f_c(E)$ are known by x-ray physics. Two measurements at different photon energy, E_L (low energy) and E_H (high energy) ,allow to determine α_p and α_c:

$$\begin{cases} \left(\frac{\mu}{\rho}\right)(E_L) = \alpha_p f_p(E_L) + \alpha_c f_c(E_L) \\ \left(\frac{\mu}{\rho}\right)(E_H) = \alpha_p f_p(E_H) + \alpha_c f_c(E_H). \end{cases} \tag{3.9}$$

This parametric fit model, since molecular interactions are not included, has limited accuracy in describing real materials. To improve the possibility of identifying different materials, two materials with well-known attenuation functions, such as water and iodine, are taken and their attenuation functions are used as basis functions. Other materials will be represented as a linear combination of them. This approach is called material decomposition. Referring to A and B to the two basis materials, from Eq. 3.8, two sets of functions can be written as follows:

$$\begin{aligned} \left(\frac{\mu}{\rho}\right)_A(E) &= \alpha_{A,p} f_p(E) + \alpha_{A,c} f_c(E), \\ \left(\frac{\mu}{\rho}\right)_B(E) &= \alpha_{B,p} f_p(E) + \alpha_{B,c} f_c(E), \end{aligned} \tag{3.10}$$

where $\alpha_{A,p}$, $\alpha_{A,c}$, $\alpha_{B,p}$, and $\alpha_{B,c}$ are the contributions of the photoelectric and Compton effects for materials A and B. Solving for $f_p(E)$ and $f_c(E)$, and substituting back into Eq.

3.8, the result is:

$$\begin{aligned}\left(\frac{\mu}{\rho}\right)(E) &= \frac{\alpha_p\alpha_{B,c}-\alpha_c\alpha_{B,p}}{\alpha_{A,p}\alpha_{B,c}-\alpha_{B,p}\alpha_{A,c}}\left(\frac{\mu}{\rho}\right)_A(E)+\frac{\alpha_c\alpha_{A,p}-\alpha_p\alpha_{A,c}}{\alpha_{A,p}\alpha_{B,c}-\alpha_{B,p}\alpha_{A,c}}\left(\frac{\mu}{\rho}\right)_B(E)= \\ &= \beta_A\left(\frac{\mu}{\rho}\right)_A(E)+\beta_B\left(\frac{\mu}{\rho}\right)_B(E).\end{aligned} \tag{3.11}$$

The previous equation (Eq. 3.11) shows that the mass attenuation coefficient of a material can be represented as the linear combination of the mass attenuation coefficients of the basis materials A and B. They have to be selected such that their effective atomic numbers Z_{eff} are sufficiently different to ensure different mass attenuation characteristics.
Multiplying both sides of Eq. 3.11 by the mass density, it yields:

$$\begin{aligned}(\mu)(E_j) &= \beta_A\left(\frac{\mu}{\rho}\right)_A(E_j)\,\rho+\beta_B\left(\frac{\mu}{\rho}\right)_B(E_j)\,\rho, && j=L,H \\ &= \left(\frac{\mu}{\rho}\right)_A(E_j)\,\rho_A+\left(\frac{\mu}{\rho}\right)_B(E_j)\,\rho_B && j=L,H.\end{aligned} \tag{3.12}$$

Two acquisitions, at low and high X-ray energy, allow us to solve the previous equations (Eq. 3.12) voxel by voxel, yielding images of the mass densities of materials A and B. This process is often called image-space material decomposition. Once Eq. 3.12 is solved, the mass density can be calculated for any energy spectra:

$$(\mu)(E_m) = \left(\frac{\mu}{\rho}\right)_A(E_m)\,\rho_A+\left(\frac{\mu}{\rho}\right)_B(E_m), \tag{3.13}$$

where $(\mu)_{A,B}(E_m)$ are the mass attenuation coefficient for the basis material A and B at the energy E_m. Images yielded by this calculation are called virtual monoenergetic images. It has been demonstrated that virtual monoenergetic images (VMI) are also the result of the weighted sum of the low- and high-energy images:

$$HU(E_m) = w(E_m)HU^L + (1-w(E_m))HU^H, \tag{3.14}$$

where HU each voxel Hounsfield Units in the low (L) and high (H) energy CT and $w(E_m)$ is the weight factor associated with the desired energy at which generate the VMI.
VMI, in radiotherapy, can be used by radiation oncologists in the target and OAR contouring; low reconstruction energy of the VMI increases the contrast between low-density tissues and thus their distinction. On the contrary, high-energy, flattened low-density tissues contrast, in favour of high-density ones. VMI can be used in proton therapy planning, passing through a CT calibration process, which does not differ from the SECT one. Evaluating the impact of the use of VMI in proton therapy dose calculation is one of the aims of this work.

3.3 Stopping Power Ratio from Dual Energy CT

Several studies have confirmed the feasibility of proton SPR extraction from DECT images. *Bär* et al. [29] have compared the most robust techniques for material decomposition developed until 2017. Each methods have developed different formalism to extract the density ρ,

or the electron density ρ_e and the effective atomic number Z_{eff} or Z_{med} from the High and Low energy images acquired with a DECT. These values are converted into I-value,the mean excitation energy of the absorbing material, via a parametric relationship.
. Obtained the I-value, the proton SPR can be calculated with Bethe's equation 2.1, dividing the resulting stopping power S by the water stopping power evaluated assuming $I_w = 73.924eV$ and a reference energy value (typically $100MeV$). Specifically, Balzova et al. [30] and Van Abbema et al.[31] approach consists in deriving ρ_e from Z_{eff} and obtaining the I-value with the conversion method proposed by Yang et al. [32]. Bourque et al. [33] introduced a different definition of the effective atomic number, Z_{med}, developing a formalism to obtain it and ρ_e and presented the Z-I conversion method, an alternative to the previous one. Whereas, Hünemohr et al. [34], Landry et al.[35] and Lalonde et al. [36] methods base their I-value estimation on the Bragg additivity rule [37](Eq. 3.15):

$$lnI = \sum_i \lambda_i lnI_i, \tag{3.15}$$

thus their formalism aims to obtain the elemental electronic fractions, λ_i, from ρ or ρ_e. All studies, excluding Balzova et al. and Van Abbema et al., require a CT calibration to determine the parameters of the model with which extract ρ or Z from a DECT and their conversion relationship.
Recently a new DECT calibration method has been developed by Viar-Hernández et al.[38]. It takes up the Bourque et al. Z-I formalism but they have implemented an alternative ρ-Z conversion based on the CT calibration.

3.3.1 DirectSPR software

DirectSPR is a software recently available on Syngo.via workstation (Siemens Healthineers, Erlangen, Germany) for the processing of Dual-Energy images acquired on Siemens DECTs. The software calculates voxel by voxel the proton stopping power ratio generating CT DICOM modality images to be exported into TPSs. It allows us to perform dose calculation on DE-derived SPR maps without needing a CT calibration and the implementation of material decomposition techniques, previously discussed.
Specifically, DirectSPR assigns to each image voxel a value equal to $1000 \times (SPR - 1)$ to give similar values as HU values. In the TPS, instead, a fictitious HU to SPR calibration curve has to be implemented to scale back to SPR units (straight line passing through the points [-1000,0] and [4000,5]).

Chapter 4

Materials and Methods

All images in this study were acquired on a Siemens Somatom go.Open Pro (Siemens Healthineers, Erlangen, Germany). For each experimental setup, a SECT image was acquired, setting, as acquisition parameters, the ones of the clinical protocols for head or body exams: 120kVp, 2 mm slice thickness, 60 cm FOV, Qr40f convolution kernel, SAFIRE iterative Reconstruction algorithm with strength 3, iMar algorithm enabled. The iBHC (iterative beam-hardening correction) bone algorithm was enabled only in the head acquisitions. The SECT scan was always followed by a DECT acquisition with a tube voltage of 80kVp and 140kVp (consecutively, being a single tube CT). The other acquisition parameters were kept unchanged. The high- and low-energy CTs were processed by the Syngo.via (version VA40) workstation to generate "Dual Energy Monoenergetic Plus" (MONO+) images (post-processed VMI) and the SPR image. The latter is an image whose voxel contains the proton SPR value computed by the DirectSPR software. SECTs, MONOs+ and SPR datasets were imported into the RayStation TPS, version 12A (RaySearch Laboratories AB, Stockholm, Sweden). SECT and MONO+ images were handled by the TPS using HU value to mass density conversion curves, derived from the tissue-substitute method and the Stoichiometric calibration for the first, Stoichiometric calibration only for the latter. Indeed, a fictitious HU to SPR curve was defined for the SPR dataset since no conversion was required.
The accuracy of the SPR assignment was investigated in terms of proton range differences between the TPS predicted and measured one. The dose was calculated separately on the SECT image, different energy MONO+ images and SPR dataset, adopting the relative conversion curves. Measurements were performed at the Proton Centre of the European Institute of Oncology (Milan, Italy), which was equipped with a PROTEUS®ONE (IBA Proton Therapy, Louvain-La-Neuve, Belgium).

4.1 Stoichiometric calibration

The Stoichiometric calibration was performed to define each HU to mass density conversion curve for SECT and MONO+ images. Specifically, MONOs+ were generated from each DE

acquisition with the following energies: 45keV, from 65keV to 90keV with steps of 5keV, 100keV, 120keV and 140keV.
To perform the SECT calibration, the first step was acquiring an X-ray SECT image of tissue equivalent samples. The Multi-Energy CT Phantom (Sun Nuclear Corporation, Melbourne, FL, USA) was used for this purpose. The phantom is a cylinder with an elliptical section made of HE CT Solid Water®(40cm x 30cm x 26.5cm), with a removable cylindrical head section of 20cm of diameter and 11 interchangeable tissue-surrogate solid plugs, plus one true water container. A phantom picture is shown in Fig. 4.1. The plug composition, provided and certified by the vendor, is reported in TAB 4.1.

Figure 4.1: Representation of the Multi-Energy CT Phantom by Sun Nuclear

X-ray CT scans were performed on the entire phantom using the clinical body protocol (body acquisition) and on the removable section using the head protocol (head acquisition). For the removable section, two images were acquired vary the plug selection to ensure at least one acquisition of each material. Separate CT calibrations were conducted for the body and head acquisitions.
Each CT image was analysed as follows: circular regions of interest (ROIs) were drawn on each plug across 20 slices in the central region of the phantom. The ROI diameter was equal to 60% of the plug one. Hounsfield Units (HU) average and standard deviation (SD) were computed for each ROI, and for each plug, the mean of these values over the slices was calculated. For redundant plugs the mean of their HU average and SD was taken.
As discussed in Sec. 3.1, plug HU averages and SDs were used to perform a linear regression and obtain the A and B parameters in Eq. 3.7. The model was applied to the 35 ICRP23 tissues and their expected HU values were obtained. Associating these HU values to the mass density of ICRP23 tissue and linearly interpolating between these points, the Stoichiometric conversion curve was obtained.
DECT scans of the entire phantom and its removable section were acquired, and MONO+

Tissue surrogate solid Plugs	**H**	**O**	**C**	**N**	**Cl**	**Ca**	**Si**	**B**	**Na**	**Mg**	ρ_r	ρ_m [g/cm^3]
Lung LN-300	7.43	20.71	57.86	1.96	0.08	0	0.77	0	0	11.19	0.29	0.3
Lung LN-450	7.44	20.69	58.03	1.97	0.08	0	0.57	0	0	11.22	0.469	0.49
HE General Adipose	9.73	14.35	71.41	2.71	0.12	0.34	1.11	0.05	0.18	0	0.949	0.96
HE Breast 50:50	9.48	15.13	70.23	2.47	0.12	0.74	1.01	0.04	0.16	0.61	0.97	0.984
True Water	11.19	88.81	0	0	0	0	0	0	0	0	1	1
He CT Solid Water	8.41	18.49	66.97	2.16	0.13	1.43	1.08	0.05	0.17	1.1	0.997	1.021
HE Brain	8.23	19.7	65.75	2.05	0.13	1.79	0.94	0.04	0.15	1.23	1.024	1.05
HE Liver	8.25	19.02	66.87	2.25	0.14	1.94	0.65	0.03	0.1	0.75	1.053	1.08
HE Inner Bone	6.38	25.64	53.79	1.73	0.1	9.82	0.72	0.03	0.11	1.68	1.151	1.201
CB2 + 30% $CaCO_3$	5.6	28.47	51.77	2.12	0.09	11.77	0	0	0	0.18	1.268	1.332
CB2 + 50% $CaCO_3$	4.03	34.13	40.34	1.52	0.07	19.62	0	0	0	0.3	1.462	1.559
HE Cortical Bone	2.31	39.95	27.41	0.85	0.04	26.62	0	0	0	2.82	1.774	1.924

Table 4.1: Summary of the Multi-Energy CT Phantom plug composition, showing the isotope percentage abundance. In the last two columns, the relative electron density (to water), ρ_r, and the mass density, ρ_m, are reported.

images were generated using the Syngo.via software. The Stoichiometric calibration procedure was applied separately to each set of images, differentiating again between body and head acquisitions. The Adjusted-R^2 values of the regression fits were taken as measure of the goodness-of-fits.

4.2 CT beam hardening effect investigation

Beam hardening is a phenomenon that occurs when an X-ray beam passes through an object, resulting in the selective attenuation of lower-energy photons, thereby hardening the energy spectrum of the beam. In CT scans, dense targets within the FOV can cause beam hardening, which may lead to characteristic artefacts such as streaking and cupping. Streaking artefacts appear as multiple dark streaks between two dense objects, while cupping artefacts manifest as regions with lower Hounsfield Unit values in the centre of the image, as the beam becomes harder in this zone compared to the periphery. Both artefacts are typically corrected automatically by the CT reconstruction algorithm. To ensure there were no residual artefacts

that could affect CT calibration, an investigation was carried out. Three SECT images of the Multi-Energy CT Phantom were acquired, varying the plug position, particularly testing configurations where the highest and lowest density plugs were placed either at the centre or the periphery of the phantom. Each CT image was analyzed using the same method applied during calibration to estimate HU averages and standard deviations. For each plug, the mean standard deviation of HU values across the different configurations was compared with the maximum difference in HU means between the three runs. The standard deviation reflects the intrinsic variability and noise level of the CT acquisition. In contrast, significant differences in HU values across the configurations could indicate the presence of residual beam hardening artefacts. The investigation was conducted on both the entire phantom using the clinical body protocol and on the removable section using the head protocol.

4.3 Virtual Monoenergetic Image noise estimation

As highlighted in the Report of AAPM Task Group 291 [20], one of the primary limitations of using virtual monoenergetic images (VMIs) is the amplification of noise caused by the material decomposition process. Increased image noise intensifies the impact of density uncertainties on dose calculations. To mitigate this, the Syngo.via software applies noise reduction techniques to VMIs, resulting in post-processed images referred to as "Dual Energy Monoenergetic Plus" (MONO+). Noise was evaluated on the same images used for the MONO+ stoichiometric calibration by measuring the HU standard deviation for each tissue-surrogate plug and comparing it to that of SECT.
It is important to note that both SECT and MONO+ images were reconstructed using clinical protocols, with no additional post-processing applied. The SECT reconstructions utilized the SAFIRE algorithm at strength level 3, designed to reduce CT radiation dose while preserving image quality. In contrast, the Dual Energy Monoenergetic Plus reconstruction algorithm focuses on denoising the images.

4.4 Proton Range investigation

4.4.1 Single pencil beam on tissue-surrogate plugs

The first experiment to investigate the accuracy of the TPS SPR assignment consisted in the comparison between calculated and measured proton ranges obtained by irradiating tissue-surrogate plugs with a single pencil beam of 226 MeV protons. The highest proton energy was selected so that the beam could pass through all the plugs and deposit the Bragg peak beyond them. SECT and DECT scans were performed on all plugs using both body and head protocols. The experimental setup, shown in Fig. 4.2 a, was constituted by the tissue-surrogate plugs of the Multi-Energy CT Phantom individually placed on a Zebra (IBA dosimetry HmbH, Schwarzenbruck, Germany) detector, along the beam direction. The Zebra is a multi-layer ion

chamber (MLIC), equipped with 180 vented ionization chambers (model PPC05), spaced at 2 mm intervals, with a 2.5 cm in diameter collecting electrode; measured range accuracy is estimated in 0.5mm, as declared in the user manual by the vendor. The experimental setup was replicated in the Raystation TPS. The dose was calculated on all the CT image configurations, SECTs, MONOs+ and SPRs, assigning the correct HU value to mass density or SPR conversion curve. To simulate the interaction of protons within the Zebra MLIC, which is water-equivalent, a box region with the dimensions of the detector was drawn in the CTs images under the plug and its density was overridden to $1 g/cm^3$, as shown in Fig. 4.2 b. For each configuration, the calculated dose matrix was processed by a Python script to obtain an integrated depth dose (IDD) comparable with the one acquired by the Zebra detector. The dose matrix was sampled along the beam direction from the top of the box region, integrating into the orthogonal directions in an area corresponding to chamber one. The Bragg Peaks were compared by evaluating the distal 90% range ($D_{90\%}R$). Additionally, a reference IDD in air with no plug present in front of the MLIC was measured and, modelling this setup on the TPS, the dose was computed. As recommended by Farace at al. [39], in this configuration, the difference between the calculated and measured $D_{90\%}R$ was determined. This offset is applied to all other IDDs in order to align coordinate systems of the MLIC measurement and TPS computation. This correction would help to eliminate setup uncertainties, ensuring that any residual differences were due only to density uncertainties.
$D_{90\%}R$ was calculated by mimicking the OmniPro-Incline software workflow (IBA dosimetry GmbH, Schwarzenbruck, Germany). The IDD was fitted using the "Bortfeld function" [40] implemented in a Python script, with $D_{90\%}R$ as one of the fit parameters. Fig. 4.3 shows a measured and a TPS calculated (on a MONO+ 75keV image) IDD, with their relative fitted Bortfeld functions. The two curves are respectively normalized to their peaks. The Zebra MLIC curve is characterised by a dose ratio between the Bragg Peak and the proximal region smaller than the calculated one as a result of the small dimension of the detector ionization chambers (PPC05). This effect does not affect the Bragg Peak depth.
To compare the performance of each SPR assignment method within them, the root mean square error (RMSE) of all the tissue-surrogate solid plug $D_{90\%}R$ differences was computed for each method.
The difference between Zebra measured $D_{90\%}R$ and $D_{90\%}R$ derived from dose calculation on SECT, MONO+ and SPR images was estimated for the different tissue-surrogate plugs.

4.4.2 Single pencil beam on animal organ samples

For the second experiment, animal organ samples were used: bovine liver, kidney, muscle and bone, swine fat and heart. Plugs have different chemical composition from human tissues and the results of the previous experiment can not be translated to clinical applications. Animal organ samples, instead, well reproduce human organs chemical composition. SECT and DECT scans of each sample were individually acquired using the body protocol. Three

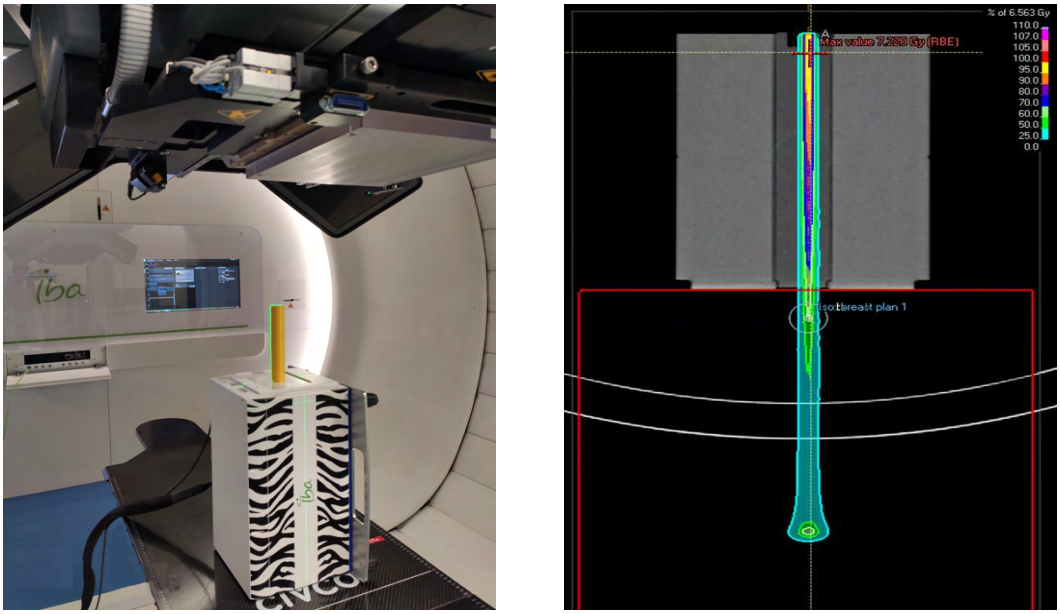

(a) (b)

Figure 4.2: The left picture shows the experimental setup for the measurements of Single Pencil Beam on tissue-surrogate plugs. The right picture shows the same setup modelled in the Raystation TPS. The dose was calculated on a CT image of the plug, overriding (to $1 g/cm^3$) the mass density of a box (red contour) under it simulating the Zebra detector.

points on the sample surface were identified as different measurement points. Similar to the previous experiment, the study aimed to investigate the difference between the measured and calculated proton ranges. The samples were irradiated with single proton pencil beams at three different energies: 100 MeV, 150 MeV and 226 MeV. The range probing was conducted with the Zebra MLIC, fixing the alignment between the beamline and the detector. The organ samples were placed on the detector, moving them to align with the three measurement points. Dose calculation and IDD analysis were performed following the same procedures as the first experiment and the $D_{90\%}R$ was taken as the estimator of the proton range. For each sample, the difference between the $D_{90\%}R$ measured with the Zebra MLIC and the $D_{90\%}R$ values derived from the TPS dose calculations on SECT, MONO+, and SPR images was estimated. The average and the standard deviation of the three values corresponding to the sample isocenters were calculated. Fig. 4.5 shows a measured and a TPS calculated (on a MONO+ 75keV image) IDD, with their relative fitted Bortfeld functions.
To compare the performance of each SPR assignment method within them, the root mean square error (RMSE) of all the tissue $D_{90\%}R$ differences was computed for each method.

4.4.3 Dose cube on animal organ samples

The animal organ samples were also irradiated with IMPT plans; two different plans were utilised: one for the bovine bone sample with higher density, and one for the other samples. These plans consisted of a 5 cm x 5 cm x 5cm (10 cm x 10 cm x 10 cm for the bone samples)

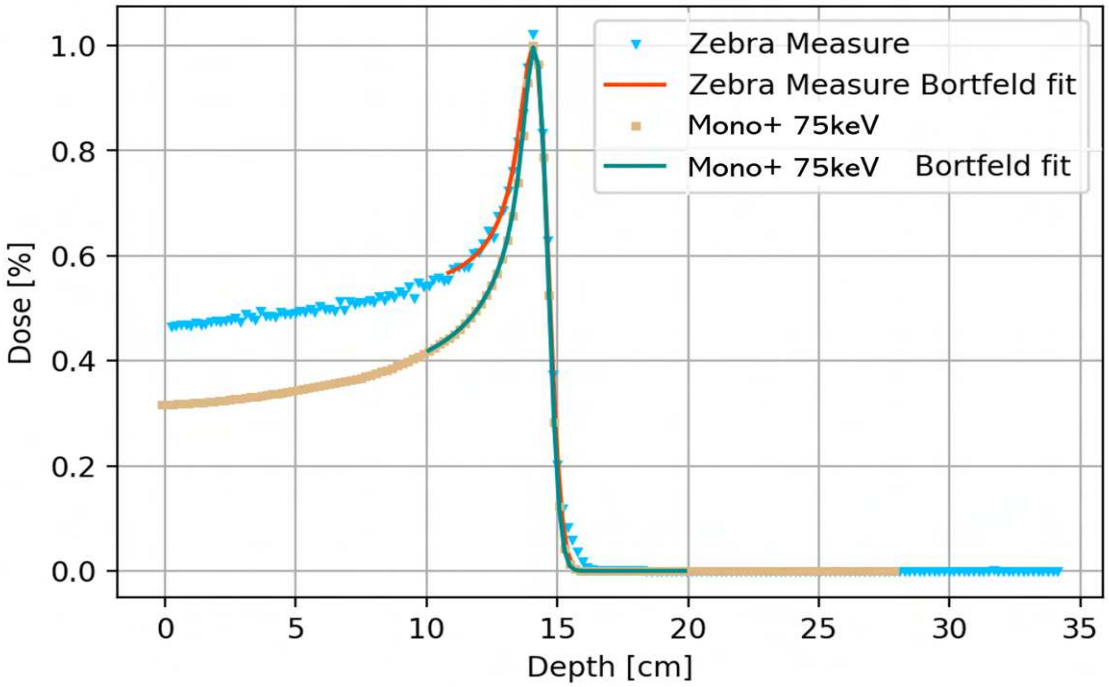

Figure 4.3: Zebra MLIC and Dual Energy Monoenergetic Plus 75keV derived IDDs processing. Distal 90% ranges are derived through a Bortfeld fit of the curves. IDDs are related to the HE Liver plug irradiation.

cube with spots uniformly distributed inside it, spaced by 4 mm (6 mm). The plans were optimised to obtain a uniform dose distribution in water within the cube. The expected $D_{90\%}R$ in water was 20 cm (30 cm). The experimental setup was the same as the previous experiment as well as its modelling on the TPS (Fig. 4.4. The measured and the TPS dose extracted IDDs did not represent Bragg Peak but SOBP. A different script in Python was developed to analyze these curves; the average dose value within the SOBP modulation region was taken as the normalization value and the $D_{90\%}R$ was obtained through a linear interpolation within points of the distal region looking for 90% of the dose. The Farace at al.'s [39] correction shift procedure was extended also to the SOBP analysis. The dose cube was delivered on the Zebra MLIC without an interposed sample and at the same time dose was computed on the TPS modelling the experimental setup.

Once again, for each sample, the difference between the $D_{90\%}R$ measured with the Zebra MLIC and the $D_{90\%}R$ values derived from the TPS dose calculations on SECT, MONO+, and SPR images was estimated. The average and the standard deviation of the three values corresponding to the sample measurement points were calculated. Fig. 4.6 shows a measured and a TPS calculated (on a MONO+ 75keV image) SOBP, with their relative R90D derivation. Differently from the single beam irradiations, the field size of the IMPT dose cube plan assures the LCPE. The two IDDs are almost overlapped.

To compare the performance of each SPR assignment method within them, the root mean

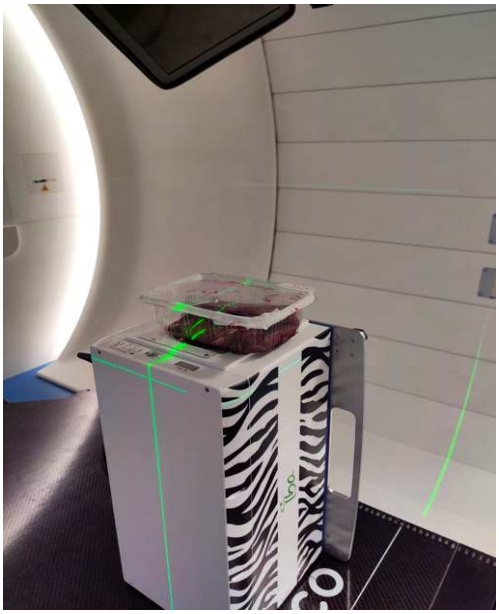

(a)

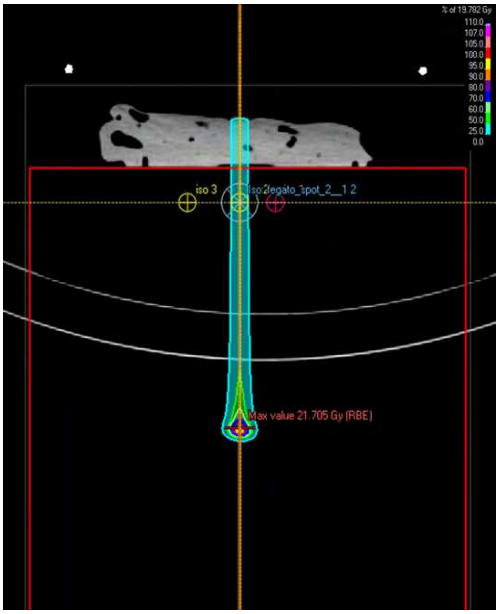

(b)

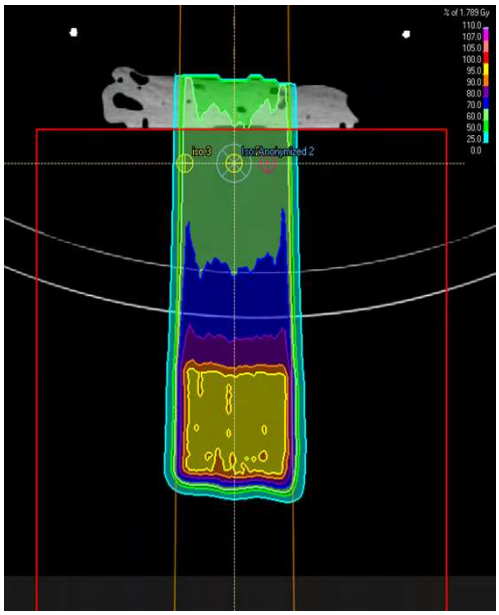

(c)

Figure 4.4: Figure (a) shows the experimental setup for the irradiation of animal organ samples. The (b) and (c) figures depict the same setup modelled in the Raystation TPS. In both the dose was calculated on CT images of the sample, overriding (to $1 g/cm^3$) the mass density of a box (red contour) under it simulating the Zebra detector. In Fig. (b), a single proton pencil beam of 150 MeV was simulated, instead, a dose cube was recomputed in Fig. (c).

square error (RMSE) of all the tissue $D_{90\%}R$ differences was computed for each method.
By restricting the analysis to SECT with the Stoichiometric calibration, 75keV DE Monoenergetic Plus with the Stoichiometric calibration and DirectSPR dataset, the density uncertainty for the various samples was estimated. It was computed as the ratio between the absolute difference from measurement and the animal organ sample thickness. Only the 75keV DE

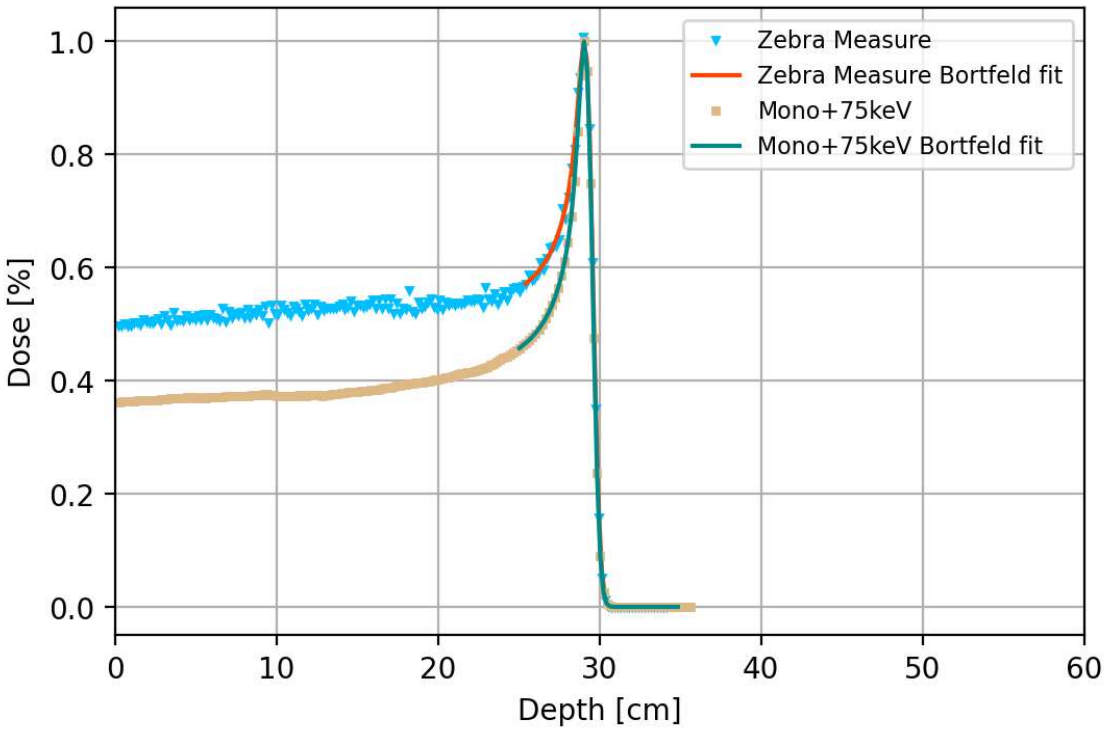

Figure 4.5: Zebra MLIC and Dual Energy Monoenergetic Plus 75keV derived IDDs processing. Distal 90% ranges are derived through a Bortfeld fit of the curves. IDDs are related to the liver sample irradiation with 266MeV proton single pencil beam.

Monoenergetic Plus was included in this comparison, within the Monoenergetic Plus images, because, as it will be shown in the results chapter (Chap. 5), it had the best agreement with measurements, although, the differences with MONO+ images reconstructed at close energy were small.

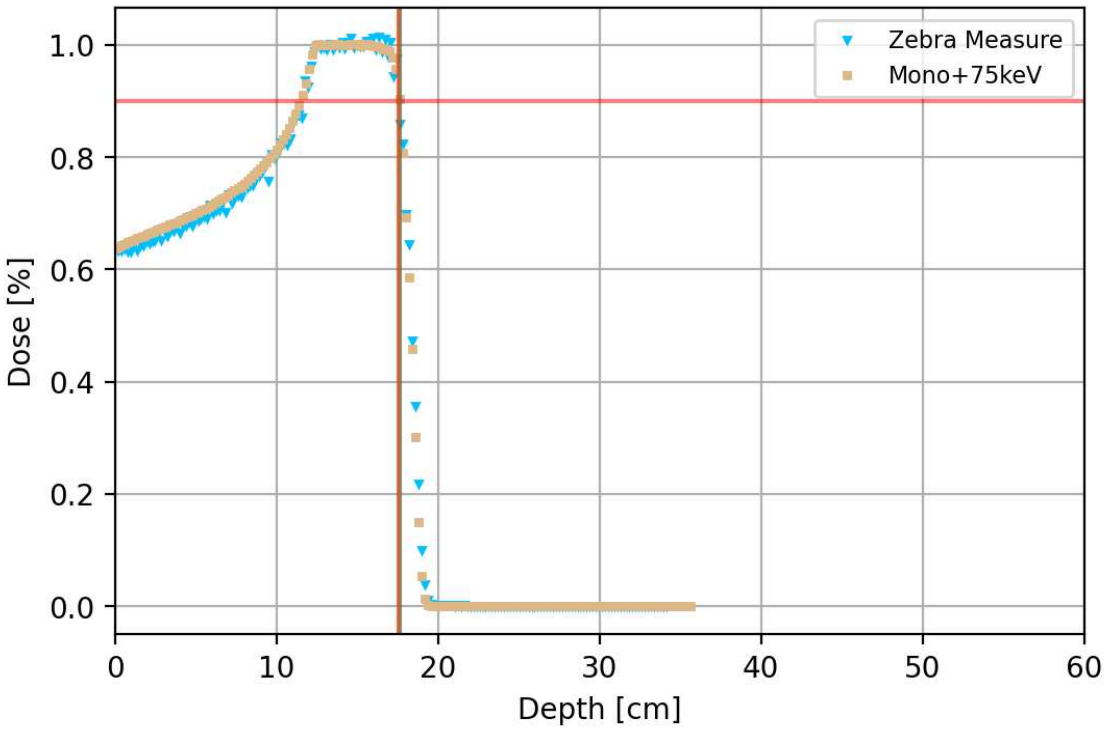

Figure 4.6: Zebra MLIC and Dual Energy Monoenergetic Plus 75keV derived IDDs processing. The interception of, respectively, the red and the green lines correspond to the Distal 90% range. IDDs are related to the liver sample irradiation with the IMPT dose cube plan.

Chapter 5

Results

5.1 CT Beam hardening effect

The results of the beam hardening investigation are presented separately for CT scans acquired using the body and head protocols, respectively in Table 5.1 and Table 5.2. For each tissue-surrogate solid plug, the mean standard deviation of HU values (HU SD), calculated across images with varying plug positions, is smaller than the maximum difference in HU means (HU Max Diff) between the three runs. This demonstrates that the CT reconstruction algorithm successfully corrected the beam hardening effect.

Tissue-surrogate solid Plug	**HU Mean**	**HU SD**	**HU Max Diff**
Lung LN-300	-688.8	28.7	7.3
Lung LN-450	-512.9	19.2	6.2
HE General Adipose	-67.1	18.4	1.7
HE Breast 50:50	-38.6	18.3	2.1
HE CT Solid Water	0.5	18.4	0.9
True Water	0.6	29.8	6.4
HE Brain	30.4	19.6	2.5
HE Liver	60.7	20.4	6.3
HE Inner Bone	283.8	17.9	1.9
CB_2 + 30% $CaCO_3$	455.9	21.7	0.8
CB_2 + 50% $CaCO_3$	820.6	22.7	10.7
HE Cortical Bone	1364.8	26.0	16.9

Table 5.1: Body acquisitions of the whole Multi-Energy CT Phantom changing the plug positions: for all tissue-surrogate solid plugs, the mean of each configuration HU value mean (HU Mean) and standard deviation (HU SD), and the maximum difference in HU means (HU Max Diff) between the three runs were evaluated and compared.

Tissue-surrogate solid Plug	HU Mean	HU SD	HU Max Diff
Lung LN-300	-702.4	27.4	0.4
Lung LN-450	-519.5	10.8	0.1
HE General Adipose	-70.0	3.9	3.5
HE Breast 50:50	-38.3	4.4	4.2
HE CT Solid Water	2.1	4.2	3.2
True Water	3.4	4.7	0.8
HE Brain	33.9	4	0.2
HE Liver	61.6	4.1	0.1
HE Inner Bone	304.9	5.5	0.1
CB_2 + 30% $CaCO_3$	489.3	7.3	1.6
CB_2 + 50% $CaCO_3$	902.1	10.9	3.5
HE Cortical Bone	1543.7	13.1	13.0

Table 5.2: Head acquisitions of the whole Multi-Energy CT Phantom changing the plug positions: for all tissue-surrogate solid plugs, the mean of each configuration HU value mean (HU Mean) and standard deviation (HU SD), and the maximum difference in HU means (HU Max Diff) between the three runs were evaluated and compared.

5.2 Virtual Monoenergetic Image Noise

The noise levels of SECT and Monoenergetic Plus images are compared in Fig. 5.1, showing the results for the entire Multi-Energy CT Phantom (a) and the head section (b) acquisition. The image noise level was estimated for each tissue-surrogate solid plug by calculating the standard deviation of the HU values. Except for the 45 keV Mono+ image, the SECT HU value SDs were approximately 100% higher than those of the Mono+ images for all plugs, with the exception of the lowest density plug, where the SDs were about 67% higher. The noise reduction method, which is implemented in the Syngo.via software, not only addresses the noise amplification issue of the VMI images but also produces images with lower noise levels than those obtained in SECT acquisitions.

5.3 Stoichiometric calibration

For simplicity, only the result of the SECT Stoichiometric calibration for the body acquisition protocol will be reported. The obtained values of the A and B parameters of the Eq. 3.7 were respectively 1.6×10^{-2} and 1.3. Figure 5.2 shows the difference between the calculated HU values using the model and the measured one for the various tissue-surrogate plugs as a function of the measured HU values. For all soft and dense plugs, the difference is between -10 and 10 HU, while for the two lung plugs, it is about -20 HU. Table 5.3 shows the Adjusted-R^2 value for all regression fits of all the stoichiometric calibrations. The obtained values were never below 0.9994, indicating the good performance of every fit. The HU values to mass

density conversion curve is shown in Fig. 5.3, along with the curve obtained using the tissue-substitute method. The Stoichiometric curve, derived from applying the regression model to the 35 ICRP23 tissues, provides a more detailed description of the conversion relationship in the soft tissue region compared to the tissue-substitute method curve, which only linearly interpolates the measured HU of six plugs. Slight differences between the two curves can be observed in the high- and low-mass density regions. Similar observations apply to the SECT Stoichiometric calibration for the head acquisition protocol and all Stoichiometric calibrations of the DE Monoenergetic Plus images.

SPR assignment methods	***Body Fit Adjusted-R^2***	***Head Fit Adujsted-R^2***
SECT	0.9997	0.9999
MONO+ 45keV	0.9994	0.9998
MONO+ 65keV	0.9996	0.9999
MONO+ 70keV	0.9996	0.9998
MONO+75keV	0.9996	0.9998
MONO+ 80keV	0.9996	0.9998
MONO+ 85keV	0.9996	0.9998
MONO+ 90keV	0.9996	0.9998
MONO+ 100keV	0.9996	0.9997
MONO+ 120keV	0.9995	0.9997
MONO+ 140keV	0.9995	0.9996

Table 5.3: Goodness-of-fit evaluation. The adjusted R^2 values of all the regression model fits of the CT images Stoichiometric calibration are reported.

5.4 Proton Range Investigation

5.4.1 Single pencil beam on tissue-surrogate plugs

Table 5.4 and Table 5.5 show the relative differences between MLIC-measured proton range and TPS prediction related to tissue-surrogate solid plug irradiation. The first table reports proton range differences derived from doses computed on SECT and DECT images acquired with the body protocol (Body), while, the latter with the head protocol (Head). In this section only MONO+ 45keV, MONO+ 75keV and MONO+ 140keV results are presented; for each plug MONO+ $D_{90\%}R$ differences are uniformly distributed between the values corresponding to the higher and the lower energies. The results related to all Monoenergetic Plus energies are shown in Tab. A.1 and Tab. A.2.

Excluding the highest density plugs, DirectSPR showed the best overall agreement with the measurements (differences within 2.7%, 1% excluding also the CB2+50%CaCO3 plug). SECT and MONO+ 75keV proton ranges differ from measurement within 1.5% for soft tissues but show differences up to 3% for low-density lung plugs and 9.5% for bone plugs. High-energy Monoenergetic Plus images compared with low energies ones had better agreement with low-density plugs measurements, but, on the contrary, wore agreement with high-density

plugs ones (excluding the highest-density one). All TPS proton ranges for the highest density plug significantly differed from the measurements (up to -32%). No major differences were highlighted when comparing the body and head results, with the first showing slightly better agreement with bone plug measurement than the seconds.
Table 5.6 compares the various SPR assignment methods' performance in terms of their RMSE of plugs $D_{90\%}R$ differences. It was computed separately including all plugs values and excluding the HE Cortical Bone one.

			Difference from MLIC $D_{90\%}R$ Measurement [mm]					
Tissue surrogate solid plugs	**Mass Density [g/cm³]**	**MLIC $D_{90\%}R$ Meas. [mm]**	**Tissue subst. SECT**	**Stoich. SECT**	**Stoich. MONO+ 45keV**	**Stoich. MONO+ 75keV**	**Stoich. MONO+ 140keV**	**DirectSPR**
Lung LN-300	0.3	270.7	2.1	-5.2	-13.3	-5.0	-1.9	-1.7
Lung LN-450	0.49	242.3	3.7	-6.6	-16.6	-6.8	-3.1	-2.4
HE General Adipose	0.96	159.9	-1.2	-1.5	-2.5	-1.9	-1.6	-1
HE Breast 50:50	0.984	156.2	-0.1	-0.2	-2.7	-0.4	-0.2	0.2
He CT Solid Water	1.021	153.0	-1.0	-2.5	-3.6	-2.0	-1.1	0.6
HE Brain	1.05	148.6	-1.4	0.1	-2.7	0.2	1.2	1.5
HE Liver	1.08	143.5	-1.4	-0.6	-2.8	-0.1	0.7	1.2
HE Inner Bone	1.201	130.1	-7.6	-8.5	-10.2	-5.6	-1.8	0.4
CB2 + 30% $CaCO_3$	1.332	109.7	-1.8	-2.2	0.1	0.1	0.1	-0.9
CB2 + 50% $CaCO_3$	1.559	82.7	-2.2	-7.7	-4.7	-3.8	-2.6	-2.3
HE Cortical Bone	1.924	39.7	-2.6	-9.5	2.9	-2.8	-9.1	-10.6

Table 5.4: The absolute differences between Zebra MLIC $D_{90\%}R$ measurements and TPS calculated $D_{90\%}R$ related to tissue-surrogate solid plug irradiation are reported. Doses were computed using DirectSPR maps, SECT images (by applying the tissue-substitute method and the Stoichiometric calibration), and Dual Energy Monoenergetic Plus images (by applying the Stoichiometric calibration) derived from CT acquisitions with the body protocol. MONO+ 45keV, MONO+ 75keV, MONO+ 140keV differences are shown; the remaining MONO+ differences are reported in table A.1

5.4.2 Animal organ sample irradiation

The results of the animal organ sample irradiation are summarised in Tab. 5.7 and 5.8, respectively referred to single pencil beam and dose cube irradiation. As in previous section, MONO+ 45keV, MONO+ 75keV and MONO+ 140keV results are presented and the datas

			Difference from MLIC $D_{90\%}R$ Measurement [mm]					
Tissue surrogate solid plugs	**Mass Density [g/cm^3]**	**MLIC $D_{90\%}R$ Meas. [mm]**	**Tissue subst. SECT**	**Stoich. SECT**	**Stoich. MONO+ 45keV**	**Stoich. MONO+ 75keV**	**Stoich. MONO+ 140keV**	**DirectSPR**
Lung LN-300	0.3	270.7	2.0	-3.6	-7.4	-3.7	-2.5	-1.4
Lung LN-450	0.49	242.3	2.7	-5.5	-11.7	-5.4	-2.5	-1.4
HE General Adipose	0.96	159.9	-2.4	-1.2	0.3	-1.6	-2.4	-1.0
HE Breast 50:50	0.984	156.2	-0.2	-0.1	-0.9	0.1	0.2	0.1
He CT Solid Water	1.021	153.0	-1.1	-0.9	-3.6	-0.9	-1.6	0.5
HE Brain	1.05	148.6	-1.8	-0.3	-1.8	0.1	1.1	1.3
HE Liver	1.08	143.5	-1.8	-0.3	-2.4	0.1	-0.2	0.8
HE Inner Bone	1.201	130.1	-4.5	-2.6	-3.5	-2.4	-2.0	-1.2
CB2 + 30% $CaCO_3$	1.332	109.7	0.6	2.4	3.2	2.2	-0.7	-1.0
CB2 + 50% $CaCO_3$	1.559	82.7	-3.0	-2.7	-1.9	-2.3	-3.3	-1.1
HE Cortical Bone	1.924	39.7	-9.0	-4.0	7.1	-0.7	-13.1	-12.0

Table 5.5: The absolute differences between Zebra MLIC $D_{90\%}R$ measurements and TPS calculated $D_{90\%}R$ related to tissue-surrogate solid plug irradiation are reported. Doses were computed using DirectSPR maps, SECT images (by applying the tissue-substitute method and the Stoichiometric calibration), and Dual Energy Monoenergetic Plus images (by applying the Stoichiometric calibration) derived from CT acquisitions with the head protocol. MONO+ 45keV, MONO+ 75keV, MONO+ 140keV differences are shown; the remaining MONO+ differences are reported in table A.2

related to all Monoenergetic Plus energies are shown in Tab. A.3 and Tab. A.4.

TPS proton range absolute differences from measurements for single pencil beam irradiation do not depend on the beam energy and they are coherent with dose cube irradiation results. TPS proton range values for all tissues slightly differs between image sets, with MONO+ 75keV showing best agreement with liver, heart and bone measurements, while DirectSPR with fat and muscles. Overall, TPS proton ranges differ from direct measurements within 1% for 226MeV proton beam and dose cube irradiation, within 1.5% for 150MeV proton beam irradiation, at most of 4% for 100MeV proton beam irradiation.

Table 5.9 compares the various SPR assignment methods' performance in terms of their RMSE of plugs $D_{90\%}R$ differences. It was computed separately for single pencil beam and dose cube irradiation data.

The density uncertainty for the various samples was determined as the ratio between the

SPR assignment methods	**RMSE Body All tissue solid plug**	**RMSE Body No HE Cortical Bone**	**RMSE Head All tissue solid plug**	**RMSE Head No HE Cortical Bone**
Tissue-sub. SECT	3.0	3.0	3.5	2.3
Stoich. SECT	5.3	4.7	2.7	2.6
Stoich. MONO+ 45keV	7.6	7.9	5.1	4.9
Stoich. MONO+ 65keV	4.2	4.4	2.8	2.9
Stoich. MONO+ 70keV	3.8	3.9	2.5	2.7
Stoich. MONO+ 75keV	3.5	3.5	2.4	2.5
Stoich. MONO+ 80keV	3.2	3.2	2.3	2.4
Stoich. MONO+ 85keV	3.1	2.9	2.4	2.3
Stoich.c MONO+ 90keV	3.0	2.6	2.6	2.2
Stoich. MONO+ 100keV	2.9	2.3	3.0	2.2
Stoich. MONO+ 120keV	3.0	1.9	3.8	2.0
Stoich. MONO+ 140keV	3.2	1.7	4.4	2.0
DirectSPR	3.5	1.4	3.8	1.2

Table 5.6: The root mean square error (RMSE) of $D_{90\%}R$ differences for each SPR assignment method. RMSE was calculated separately including all the tissue-surrogate solid plugs $D_{90\%}R$ differences and excluding the HE Cortical Bone one.

proton range absolute difference from measurement and the animal organ sample thickness. Table 5.10 summarises the results of the density uncertainty evaluation for SECT with the Stoichiometric calibration, 75 keV DE Monoenergetic Plus with the Stoichiometric calibration and DirectSPR dataset.

		Difference from MLIC $D_{90\%}R$ Measurement: Mean ± SD [mm]						
Tissue	**Beam Energy [MeV]**	**MLIC $D_{90\%}R$ Meas. Mean ± SD [mm]**	**Tissue subst. SECT**	**Stoich. SECT**	**Stoich. MONO+ 45keV**	**Stoich. MONO+ 75keV**	**Stoich. MONO+ 140keV**	**DirectSPR**
Liver	100MeV	50.3 ± 1.5	-0.4 ± 0.4	-0.4 ± 0.4	-0.7 ± 0.4	-0.4 ± 0.4	-0.3 ± 0.4	-0.3 ± 0.4
Liver	150MeV	130.9 ± 1.6	-0.4 ± 0.5	-0.5 ± 0.5	-0.8 ± 0.5	-0.5 ± 0.5	-0.4 ± 0.5	-0.4 ± 0.5
Liver	226MeV	292.2 ± 1.6	-0.2 ± 0.6	-0.3 ± 0.6	-0.6 ± 0.6	-0.3 ± 0.6	-0.2 ± 0.6	-0.2 ± 0.6
Heart	100MeV	20.4 ± 7.1	0.3 ± 0.8	0.3 ± 0.9	-0.6 ± 0.4	0.8 ± 0.7	1.1 ± 0.5	1.1 ± 0.5
Heart	150MeV	100.3 ± 6.6	-0.1 ± 0.5	0.0 ± 0.4	-0.8 ± 0.5	0.3 ± 0.4	0.8 ± 0.5	0.7 ± 0.4
Heart	226MeV	261.5 ± 6.4	0.1 ± 0.6	0.2 ± 0.5	-0.6 ± 0.5	0.5 ± 0.5	0.9 ± 0.6	0.8 ± 0.5
Bone	150MeV	78.4 ± 3.7	-1.7 ± 0.2	-2.9 ± 0.4	-1.3 ± 0.3	0.0 ± 0.3	1.1 ± 0.0	1.0 ± 0.1
Bone	226MeV	239.2 ± 3.7	-1.4 ± 0.4	-2.7 ± 0.5	-1.0 ± 0.4	0.3 ± 0.4	1.4 ± 0.2	1.2 ± 0.1
Fat	100MeV	37.6 ± 3.5	1.9 ± 0.7	1.3 ± 0.8	1.1 ± 0.9	1.0 ± 0.9	1.0 ± 0.9	0.8 ± 0.9
Fat	150MeV	118.0 ± 3.6	2.2 ± 0.8	1.7 ± 0.8	1.5 ± 0.8	1.4 ± 0.9	1.4 ± 0.9	1.3 ± 0.9
Fat	226MeV	279.3 ± 3.8	2.5 ± 0.8	2.1 ± 0.8	1.9 ± 0.8	1.8 ± 0.9	1.8 ± 0.9	1.7 ± 0.9
Kidney	100MeV	40.4 ± 2.5	-1.9 ± 2.1	-1.8 ± 2.2	-1.8 ± 1.9	-1.5 ± 2.0	-1.3 ± 2.0	-1.5 ± 2.1
Kidney	150MeV	119.9 ± 2.1	-0.9 ± 1.0	-0.9 ± 1.0	-1.0 ± 1.1	-0.6 ± 1.0	-0.4 ± 1.1	-0.5 ± 1.0
Kidney	226MeV	281.3 ± 2.1	-0.5 ± 1.1	-0.5 ± 1.1	-0.6 ± 1.2	-0.2 ± 1.2	0.0 ± 1.2	-0.1 ± 1.2
Muscle	100MeV	30.8 ± 3.7	-0.9 ± 0.2	-0.9 ± 0.2	-1.1 ± 0.3	-0.7 ± 0.3	-0.6 ± 0.2	-0.6 ± 0.2
Muscle	150MeV	110.7 ± 3.8	-0.9 ± 0.4	-0.9 ± 0.4	-1.1 ± 0.5	-0.7 ± 0.4	-0.6 ± 0.4	-0.6 ± 0.4
Muscle	226MeV	272.0 ± 3.8	-0.7 ± 0.5	-0.7 ± 0.4	-0.9 ± 0.5	-0.5 ± 0.5	-0.4 ± 0.5	-0.4 ± 0.4

Table 5.7: The absolute differences between Zebra MLIC $D_{90\%}R$ measurements and TPS calculated $D_{90\%}R$ related to animal organ samples single spot irradiation are reported. Doses were computed using DirectSPR maps, SECT images (by applying the tissue-substitute method and the Stoichiometric calibration), and Dual Energy Monoenergetic Plus images (by applying the Stoichiometric calibration). MONO+ 45keV, MONO+ 75keV, MONO+ 140keV differences are shown; the remaining MONO+ differences are reported in table A.3

		Difference from MLIC $D_{90\%}R$ Measurement: Mean ± SD [mm]					
Tissue	**MLIC $D_{90\%}R$ Meas. Mean ± SD [mm]**	**Tissue subst. SECT**	**Stoich. SECT**	**Stoich. MONO+ 45keV**	**Stoich. MONO+ 75keV**	**Stoich. MONO+ 140keV**	**DirectSPR**
Liver	175.0 ± 1.6	0.6 ± 0.2	0.6 ± 0.2	0.2 ± 0.3	0.5 ± 0.2	0.7 ± 0.3	0.7 ± 0.2
Heart	146.1 ± 5.6	-0.7 ± 1.2	-0.5 ± 1.3	-1.3 ± 1.3	-0.1 ± 1.3	0.3 ± 1.4	0.2 ± 1.4
Bone	225.9 ± 4.2	-0.9 ± 0.6	-2.2 ± 0.5	-0.4 ± 0.8	0.9 ± 0.8	1.9 ± 0.9	1.7 ± 0.9
Fat	163.2 ± 1.5	2.3 ± 1.1	1.9 ± 1.1	1.8 ± 1.1	1.7 ± 1.2	1.7 ± 1.2	1.4 ± 1.1
Kidney	163.8 ± 0.6	-0.8 ± 0.4	-0.8 ± 0.4	-1.4 ± 0.4	-0.7 ± 0.4	-0.5 ± 0.4	-0.4 ± 0.4
Muscle	156.5 ± 2.9	0.2 ± 0.7	0.3 ± 0.7	0.1 ± 0.7	0.4 ± 0.7	0.5 ± 0.7	0.4 ± 0.7

Table 5.8: The absolute differences between Zebra MLIC $D_{90\%}R$ measurements and TPS calculated $D_{90\%}R$ related to animal organ samples dose cube irradiation are reported. Doses were computed using DirectSPR maps, SECT images (by applying the tissue-substitute method and the Stoichiometric calibration), and Dual Energy Monoenergetic Plus images (by applying the Stoichiometric calibration). MONO+ 45keV, MONO+ 75keV, MONO+ 140keV differences are shown; the remaining MONO+ differences are reported in table A.4

SPR assignment methods	RMSE Animal Sample Single Pencil Beam	RMSE Animal Sample Dose Cube
Tissue-sub. SECT	1.3	1.1
Stoich. SECT	1.4	1.3
Stoich. MONO+ 45keV	1.1	1.1
Stoich. MONO+ 65keV	0.8	0.9
Stoich. MONO+ 70keV	0.8	0.9
Stoich. MONO+ 75keV	0.8	0.9
Stoich. MONO+ 80keV	0.8	0.9
Stoich. MONO+ 85keV	0.8	1.0
Stoich. MONO+ 90keV	0.9	1.0
Stoich. MONO+ 100keV	0.9	1.0
Stoich. MONO+ 120keV	0.9	1.1
Stoich. MONO+ 140keV	0.9	1.1
DirectSPR	0.9	1.0

Table 5.9: The root mean square error (RMSE) of $D_{90\%}R$ differences for each SPR assignment method. RMSE was calculated separately including the $D_{90\%}R$ differences obtained from single pencil beam and dose cube irradiation of tissus animal samples.

		Density Uncertainty [%]		
Tissue	**Thickness [mm]**	**Stoich. SECT**	**Stoich. MONO+ 75keV**	**DirectSPR**
Liver	25	2.0 ± 0.8	2.0 ± 0.8	2.8 ± 0.8
Heart	59	-0.5 ± 2.2	-0.2 ± 2.2	0.3 ± 2.4
Bone	61	0.8 ± 1.3	1.5 ± 1.3	2.8 ± 1.5
Fat	44	3.9 ± 2.7	3.9 ± 2.7	3.2 ± 2.5
Kidney	43	-1.9 ± 0.9	-1.6 ± 0.9	-0.9 ± 0.9
Muscle	48	0.8 ± 1.5	0.8 ± 1.5	0.8 ± 1.5

Table 5.10: Density uncertainty estimation for various animal organ samples. Three SPR assignment methods are compared: SECT with the Stoichiometric calibration, DE Monoenergetic Plus with the Stoichiometric calibration and DirectSPR dataset.

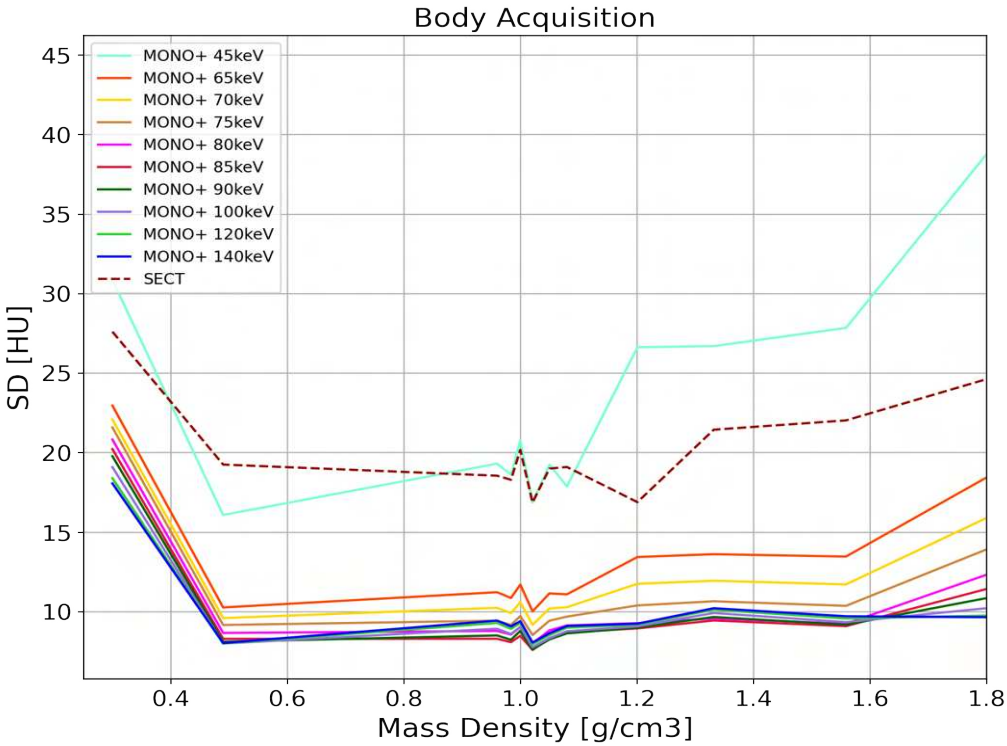

(a)

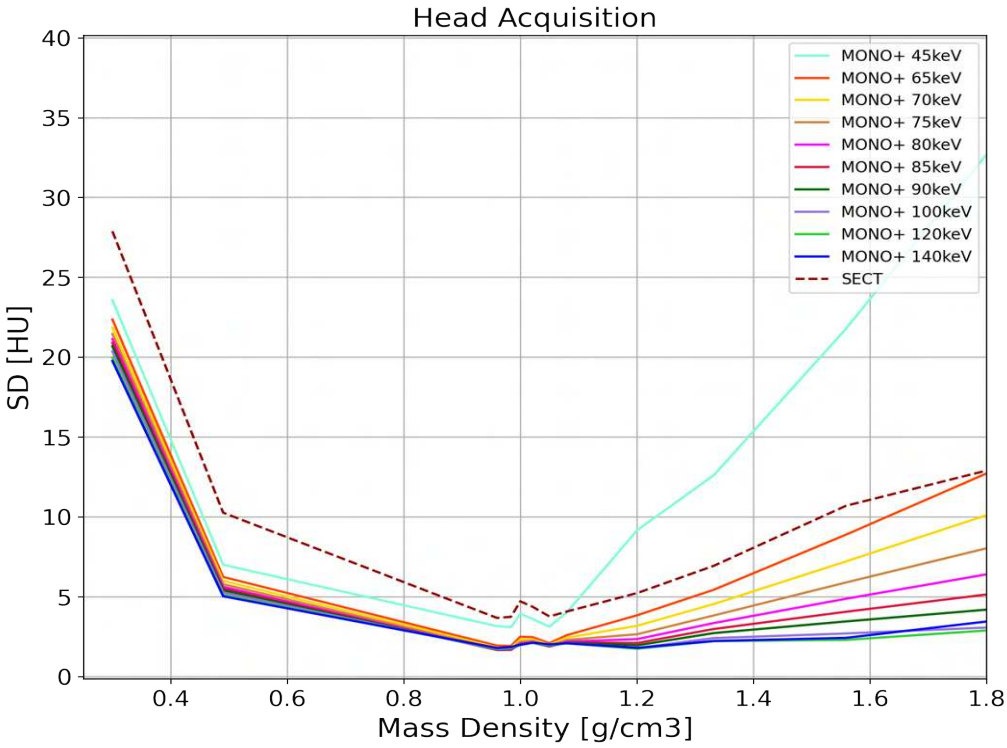

(b)

Figure 5.1: Standar Deviation of HU values as a function of the electron density of all the tissue-surrogate solid plugs of the Multi-Energy CT Phantom evaluated on SECT and different keV Monoenergetic Plus images. Figure (a) shows the results related to the whole Multi-Energy CT Phantom acquisitions, instead Figure (b) to the head section images.

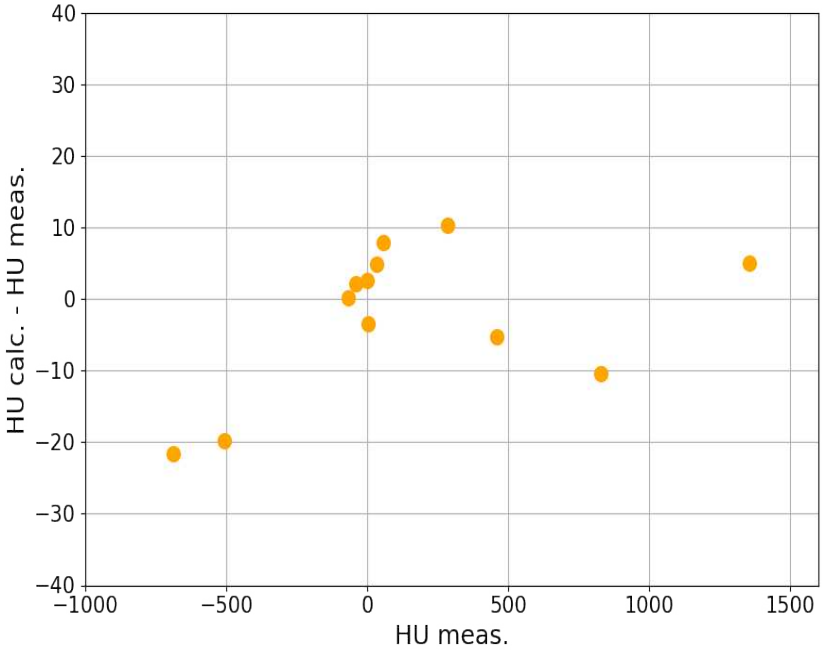

Figure 5.2: Differences between the calculated HU values using the Body SECT regression model and the measured one for the various tissue-surrogate plugs as a function of the measured HU.

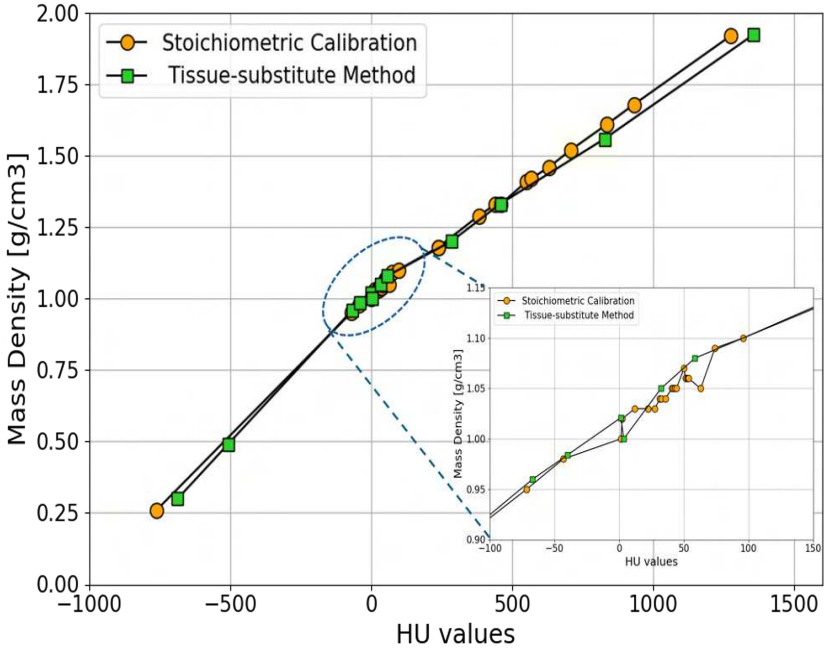

Figure 5.3: HU values to mass density conversion curves obtained through the Stoichiometric calibration and the Tissue-substitute method for SECT images acquired with the body protocol.

Chapter 6

Discussion

X-ray CTs are imperfect but (currently) irreplaceable inputs for proton dose calculation. HU values are a measure of the photon attenuation and deriving from them the SPR and the material composition to assign to each voxel is error-prone. The conversion relationship is not unique; generally, TPSs perform this assignment using an HU value to mass density or SPR conversion curve to choose the closest material composition and physical property from a template list.
DECTs and commercial software able to calculate SPR from two different energy CT acquisitions are now technologically mature. Multiple previous studies [4–7] examined the feasibility of using SPR data generated from DECT. These studies demonstrated the higher agreement of DE SPR with the value extracted from proton range measurement than the one derived from SECTs through the conversion curves.
This study, instead, focused on the accuracy of the proton range prediction depending on the image set used for the dose calculation. Dose calculation on SPR maps is a recently added feature on TPSs. The various SPR prediction approaches were compared including the TPS material assignment, being its role not negligible on the final dosimeter output.

The tissue-surrogate solid plug irradiation confirmed the behaviour highlighted by the SPR assignment studies. DirectSPR proton ranges showed a better agreement with measurements than CT calibration-based methods, both SECT and Dual Energy Monoenergetic Plus. The same plugs used for CT calibrations were employed in this investigation, which may have influenced the results. In fact, the greatest discrepancies in proton range were observed in plugs where the regression model (Fig. 5.2) was less accurate. All the TPS calculated proton ranges significantly differed (up to 32%) from the measurement for the He Cortical Bone plug. However, the adjusted-R^2 evaluation assesses the goodness-of-fit of all calibration regression procedures. This study focused on tissue-like materials, but the absence of higher-density plugs, such as titanium (which are commercially available), may have impacted the accuracy of the CT calibration curves in the higher-density range. For materials with HU values higher than those of the He Cortical Bone plug, the conversion is based on linear extrapolation from

the two highest-density points in the model.
DirectSPR conversions, instead, are not based on CT calibration. Its SPR assignment showed a 1% agreement with proton range measurements for all but the high-density plugs. High-density materials may present a limitation for this software, further investigation is needed.

TPS-calculated proton ranges were compared with measured values by irradiating tissue samples with a single pencil beam at various energies. The absolute differences between TPS proton ranges and measurements did not depend on beam energy. DirectSPR proton ranges differed from the measured values by no more than 1.5% for proton beams at 150 MeV and 226 MeV, showing good agreement with the results of Sarkar et al. [41] for the same organ samples. In their study, a significant difference of approximately 2 mm was observed between SECT and DirectSPR proton ranges, while our results showed a maximum difference of only 0.7 mm. This discrepancy may be attributed to differences in experimental setup. Sarkar et al. grounded their samples to create a homogeneous compound, whereas we scanned and irradiated whole pieces of tissue to preserve and investigate their intrinsic inhomogeneity. The variability of SPR value within the sample may flatten the total proton range difference between the different SPR assignment methods. In addition, they do not implement a SECT stoichiometric calibration which increases the accuracy of the method.
The 75 keV Monoenergetic Plus images showed better agreement with measurements compared to SECT. Both SPR assignments were based on stoichiometric calibration, and the conversion curves derived from the two methods were similar. This result highlights the impact of different noise levels in the images, which depend on the reconstruction and/or denoising algorithms applied. The Syngo.via software used for generating Monoenergetic Plus images was more effective at reducing noise than the SAFIRE algorithm (strength 3) used for SECT. Aside from SAFIRE, no additional noise reduction techniques were available for SECT reconstruction on the used CT scanner. In this study, images were generated only following the clinical protocol. This may be a limitation and in future investigations other noise reduction techniques [42] should be inspected.
The irradiation of animal organ samples using simple IMPT plans was conducted to better simulate clinical treatment conditions. The density uncertainty observed for the fat sample, which was larger and showed low repeatability (indicated by a high standard deviation), suggests the presence of setup errors. These errors could be due to misalignment with the beamline or changes in the sample between CT acquisition and irradiation. Excluding the fat sample, a density uncertainty of around 2% can be associated with the use of SECT and 75 keV Monoenergetic Plus images, along with their respective stoichiometric calibration curves, for proton dose calculations.
Unexpectedly, the density uncertainty for DirectSPR was higher at 2.8%, which warrants further investigation to better understand this result. Although preliminary, the findings of this study support the recommendations of several authors, such as Peters et al. [43], to lower the clinical density uncertainty from 3.5% when using DECT SPR assignment methods.

However, this study has more limitations that should be discussed. Low-density tissue samples, such as lungs, were not included in this study. The large standard deviations indicate the need for improved setup repeatability in future investigations, as sub-millimetre accuracy is essential for proton range measurements. One potential strategy could be to minimize the time between CT scanning and irradiation, use rigid plastic containers to stabilize the animal tissue samples, and increase their thickness to create proton range differences that exceed measurement errors. For clinical implementation of DECT acquisitions using single-tube CT scanners like the Siemens Somatom go.Open Pro, the impact of image artefacts caused by patient motion, whether unintentional or intentional, between the two energy scans should also be investigated.

Chapter 7

Conclusion

The results of this study confirm the feasibility of the use of DirectSPR and Monoenergetic Plus images generated by the Syngo.via software as input to the Raystation TPS for proton dose calculation. The impact of various methods of SPR assignment was evaluated: the tissue substitute method on SECT images, the stoichiometric calibration on SECT and Monoenergetic Plus images and the DirectSPR dataset.

Proton range measurements using tissue surrogate solid plugs confirmed the greater accuracy of DirectSPR prediction than the other methods. This result was consistent with previous SPR assignment studies. However, the software showed lower accuracy for high-density materials, indicating the need for further investigation before it can be fully integrated into clinical protocols.

The comparison of measured proton ranges of animal organ samples and TPS calculation revealed a less pronounced difference between SPR assignment methods, and for certain tissues, it did not confirm the superior accuracy of DirectSPR. A density uncertainty of approximately 2% can be associated with SECT and 75 keV Monoenergetic Plus images for proton dose calculation, while DirectSPR showed a higher uncertainty at 2.8%.

Although preliminary, the results of this study support the reduction of the 3.5% clinical density uncertainty enabled by the implementation of dual-energy CT as suggested by many authors.

Appendix A

Appendix A

			Difference from MLIC D90R Measurement [mm]			
Tissue surrogate solid plugs	**Mass Density [g/cm^3]**	**MLIC D90R Meas. [mm]**	**Stoich. MONO+ 45keV**	**Stoich. MONO+ 65keV**	**Stoich. MONO+ 70keV**	**Stoich. MONO+ 75keV**
Lung LN-300	0.3	270.7	-13.3	-6.6	-5.7	-5.0
Lung LN-450	0.49	242.3	-16.6	-8.6	-.6	-6.8
HE General Adipose	0.96	159.9	-2.5	-2.0	-2.0	-1.9
HE Breast 50:50	0.984	156.2	-2.7	-0.7	-0.6	-0.4
He CT Solid Water	1.021	153.0	-3.6	-1.2	-1.2	-2.0
HE Brain	1.05	148.6	-2.7	-0.4	-0.1	0.2
HE Liver	1.08	143.5	-2.8	-0.9	-0.5	-0.1
HE Inner Bone	1.201	130.1	-10.2	-7.1	-6.3	-5.6
CB2 + 30% $CaCO_3$	1.332	109.7	0.1	0.1	0.1	0.1
CB2 + 50% $CaCO_3$	1.559	82.7	-4.7	-4.1	-4.0	-3.8
HE Cortical Bone	1.924	39.7	2.9	-0.9	-1.9	-2.8

Tissue surrogate solid plugs	Mass Density [g/cm^3]	MLIC D90R Meas. [mm]	Difference from MLIC D90R Measurement [mm]					
			Stoich. MONO+ 80keV	Stoich. MONO+ 85keV	Stoich. MONO+ 90keV	Stoich. MONO+ 100keV	Stoich. MONO+ 120keV	Stoich. MONO+ 140keV
Lung LN-300	0.3	270.7	-4.4	-3.9	-3.5	-3.0	-2.3	-1.9
Lung LN-450	0.49	242.3	-6.1	-5.6	-5.1	-4.5	-3.6	-3.1
HE General Adipose	0.96	159.9	-1.8	-1.8	-1.8	-1.7	-1.6	-1.6
HE Breast 50:50	0.984	156.2	-0.3	-0.1	0.1	0.1	0.1	-0.2
He CT Solid Water	1.021	153.0	-1.7	-1.5	-1.4	-1.3	-1.2	-1.1
HE Brain	1.05	148.6	0.5	0.7	0.8	1.0	1.2	1.2
HE Liver	1.08	143.5	0.1	0.3	0.5	-0.2	0.4	0.7
HE Inner Bone	1.201	130.1	-4.9	-4.3	-3.7	-2.8	-2.1	-1.8
CB2 + 30% $CaCO_3$	1.332	109.7	0.1	0.1	0.1	0.1	0.1	0.1
CB2 + 50% $CaCO_3$	1.559	82.7	-3.7	-3.5	-3.4	-3.1	-2.8	-2.6
HE Cortical Bone	1.924	39.7	-3.7	-4.4	-5.1	-6.3	-8.0	-9.1

Table A.1: The absolute differences between Zebra MLIC D90R measurements and Dual Energy Monoenergetic Plus images calculated D90R related to tissue surrogate solid plug irradiation are reported. Doses were computed using images derived from CT acquisitions with the abdomen protocol.

			Difference from MLIC D90R Measurement [mm]			
Tissue surrogate solid plugs	**Mass Density [g/cm^3]**	**MLIC D90R Meas. [mm]**	**Stoich. MONO+ 45keV**	**Stoich. MONO+ 65keV**	**Stoich. MONO+ 70keV**	**Stoich. MONO+ 75keV**
Lung LN-300	0.3	270.7	-7.4	-4.3	-4.0	-3.7
Lung LN-450	0.49	242.3	-11.7	-6.6	-5.9	-5.4
HE General Adipose	0.96	159.9	0.3	-1.2	-1.4	-1.6
HE Breast 50:50	0.984	156.2	-0.9	-0.1	-0.1	-0.1
He CT Solid Water	1.021	153.0	-3.6	-0.8	-0.8	-0.9
HE Brain	1.05	148.6	-1.8	-0.5	-0.2	0.1
HE Liver	1.08	143.5	-2.4	-0.2	0.1	0.1
HE Inner Bone	1.201	130.1	-3.5	-2.7	-2.5	-2.4
CB2 + 30% $CaCO_3$	1.332	109.7	3.2	2.8	2.5	2.2
CB2 + 50% $CaCO_3$	1.559	82.7	-1.9	-2.1	-2.2	-2.3
HE Cortical Bone	1.924	39.7	7.1	2.0	0.6	-0.7

Tissue surrogate solid plugs	Mass Density [g/cm^3]	MLIC D90R Meas. [mm]	Difference from MLIC D90R Measurement [%]					
			Stoich. MONO+ 80keV	Stoich. MONO+ 85keV	Stoich. MONO+ 90keV	Stoich. MONO+ 100keV	Stoich. MONO+ 120keV	Stoich. MONO+ 140keV
Lung LN-300	0.3	270.7	-3.4	-3.3	-3.1	-2.9	-2.7	-2.5
Lung LN-450	0.49	242.3	-5.0	-4.7	-4.5	-4.1	-3.5	-3.3
HE General Adipose	0.96	159.9	-1.7	-1.8	-1.9	-2.1	-2.3	-2.4
HE Breast 50:50	0.984	156.2	0.1	-0.1	0.1	0.1	0.2	0.2
He CT Solid Water	1.021	153.0	-1.0	-1.1	-1.3	-1.5	-1.6	-1.6
HE Brain	1.05	148.6	0.4	0.6	0.7	0.9	1.0	1.1
HE Liver	1.08	143.5	0.2	0.3	0.4	-0.7	-0.4	-0.2
HE Inner Bone	1.201	130.1	-2.3	-2.2	-2.2	-2.2	-2.1	-2.0
CB2 + 30% $CaCO_3$	1.332	109.7	1.8	1.5	1.2	0.6	-0.1	-0.7
CB2 + 50% $CaCO_3$	1.559	82.7	-2.4	-2.6	-2.8	-2.9	-2.9	-3.3
HE Cortical Bone	1.924	39.7	-2.2	-3.6	-4.9	-7.3	-10.7	-13.1

Table A.2: The absolute differences between Zebra MLIC D90R measurements and Dual Energy Monoenergetic Plus images calculated D90R related to tissue surrogate solid plug irradiation are reported. Doses were computed using images derived from CT acquisitions with the head protocol.

			Difference from MLIC D90R Measurement: Mean ± STD [mm]				
Tissue	**Beam Energy [MeV]**	**MLIC D90R Meas. Mean ± STD [mm]**	**Stoich. MONO+ 45keV**	**Stoich. MONO+ 65keV**	**Stoich. MONO+ 70keV**	**Stoich. MONO+ 75keV**	**Stoich. MONO+ 80keV**
Liver	100MeV	50.3 ± 1.5	-0.7 ± 0.4	-0.5 ± 0.4	-0.5 ± 0.4	-0.4 ± 0.4	-0.4 ± 0.4
Liver	150MeV	130.9 ± 1.6	-0.8 ± 0.5	-0.6 ± 0.5	-0.6 ± 0.5	-0.5 ± 0.5	-0.5 ± 0.5
Liver	226MeV	292.2 ± 1.6	-0.6 ± 0.6	-0.4 ± 0.6	-0.3 ± 0.6	-0.3 ± 0.6	-0.3 ± 0.6
Heart	100MeV	20.4 ± 7.1	-0.6 ± 0.4	0.3 ± 0.9	0.4 ± 0.9	0.8 ± 0.7	0.8 ± 0.5
Heart	150MeV	100.3 ± 6.6	-0.8 ± 0.5	0.1 ± 0.5	0.3 ± 0.4	0.3 ± 0.4	0.4 ± 0.4
Heart	226MeV	261.5 ± 6.4	-0.6 ± 0.5	0.3 ± 0.5	0.4 ± 0.5	0.5 ± 0.5	0.6 ± 0.5
Bone	150MeV	78.4 ± 3.7	-1.3 ± 0.3	-0.3 ± 0.3	-0.2 ± 0.3	0.0 ± 0.3	0.2 ± 0.2
Bone	226MeV	239.2 ± 3.7	-1.0 ± 0.4	-0.0 ± 0.4	0.2 ± 0.4	0.3 ± 0.4	0.5 ± 0.4
Fat	100MeV	37.6 ± 3.5	1.1 ± 0.9	1.0 ± 0.9	1.0 ± 0.9	1.0 ± 0.9	1.0 ± 0.9
Fat	150MeV	118.0 ± 3.6	1.5 ± 0.8	1.4 ± 0.9	1.4 ± 0.9	1.4 ± 0.9	1.4 ± 0.9
Fat	226MeV	279.3 ± 3.8	1.9 ± 0.8	1.8 ± 0.9	1.8 ± 0.9	1.8 ± 0.9	1.8 ± 0.9
Kydney	100MeV	40.4 ± 2.5	-1.8 ± 1.9	-1.6 ± 1.9	-1.5 ± 2.0	-1.5 ± 2.0	-1.5 ± 2.0
Kydney	150MeV	119.9 ± 2.1	-1.0 ± 1.1	-0.7 ± 1.0	-0.6 ± 1.0	-0.6 ± 1.0	-0.6 ± 1.0
Kydney	226MeV	281.3 ± 2.1	-0.6 ± 1.2	-0.2 ± 1.2	-0.2 ± 1.2	-0.2 ± 1.2	-0.1 ± 1.2
Muscle	100MeV	30.8 ± 3.7	-1.1 ± 0.3	-0.8 ± 0.3	-0.8 ± 0.3	-0.7 ± 0.3	-0.7 ± 0.2
Muscle	150MeV	110.7 ± 3.8	-1.1 ± 0.5	-0.8 ± 0.5	-0.7 ± 0.5	-0.7 ± 0.4	-0.6 ± 0.4
Muscle	226MeV	272.0 ± 3.8	-0.9 ± 0.5	-0.6 ± 0.5	-0.6 ± 0.5	-0.5 ± 0.5	-0.5 ± 0.4

			Difference from MLIC D90R Measurement: Mean ± STD [mm]				
Tissue	**Beam Energy [MeV]**	**MLIC D90R Meas. Mean ± STD [mm]**	**Stoich. MONO+ 85keV**	**Stoich. MONO+ 90keV**	**Stoich. MONO+ 100keV**	**Stoich. MONO+ 120keV**	**Stoich. MONO+ 140keV**
Liver	100MeV	50.3 ± 1.5	-0.4 ± 0.4	-0.4 ± 0.4	-0.4 ± 0.4	-0.3 ± 0.4	-0.3 ± 0.4
Liver	150MeV	130.9 ± 1.6	-0.5 ± 0.5	-0.5 ± 0.5	-0.4 ± 0.5	-0.4 ± 0.5	-0.4 ± 0.5
Liver	226MeV	292.2 ± 1.6	-0.3 ± 0.6	-0.3 ± 0.6	-0.2 ± 0.6	-0.2 ± 0.6	-0.2 ± 0.6
Heart	100MeV	20.4 ± 7.1	0.8 ± 0.5	0.9 ± 0.6	0.9 ± 0.6	1.0 ± 0.5	1.1 ± 0.5
Heart	150MeV	100.3 ± 6.6	0.5 ± 0.4	0.5 ± 0.4	0.5 ± 0.5	0.7 ± 0.5	0.8 ± 0.5
Heart	226MeV	261.5 ± 6.4	0.6 ± 0.5	0.7 ± 0.5	0.6 ± 0.6	0.9 ± 0.6	0.9 ± 0.6
Bone	150MeV	78.4 ± 3.7	0.3 ± 0.2	0.4 ± 0.2	0.6 ± 0.1	0.9 ± 0.1	1.1 ± 0.0
Bone	226MeV	239.2 ± 3.7	0.6 ± 0.3	0.8 ± 0.3	0.9 ± 0.3	1.2 ± 0.2	1.4 ± 0.2
Fat	100MeV	37.6 ± 3.5	1.0 ± 0.9	1.0 ± 0.9	1.0 ± 0.9	1.0 ± 0.9	1.0 ± 0.9
Fat	150MeV	118.0 ± 3.6	1.4 ± 0.9	1.4 ± 0.9	1.4 ± 0.9	1.4 ± 0.9	1.4 ± 0.9
Fat	226MeV	279.3 ± 3.8	1.8 ± 0.9	1.8 ± 0.9	1.8 ± 0.9	1.8 ± 0.9	1.8 ± 0.9
Kydney	100MeV	40.4 ± 2.5	-1.4 ± 2.0	-1.4 ± 2.0	-1.4 ± 2.0	-1.3 ± 2.0	-1.3 ± 2.0
Kydney	150MeV	119.9 ± 2.1	-0.5 ± 1.0	-0.5 ± 1.0	-0.5 ± 1.1	-0.4 ± 1.1	-0.4 ± 1.1
Kydney	226MeV	281.3 ± 2.1	-0.1 ± 1.2	-0.1 ± 1.2	-0.1 ± 1.2	0.0 ± 1.2	0.0 ± 1.2
Muscle	100MeV	30.8 ± 3.7	-0.7 ± 0.2	-0.7 ± 0.2	-0.7 ± 0.2	-0.6 ± 0.2	-0.6 ± 0.2
Muscle	150MeV	110.7 ± 3.8	-0.6 ± 0.4	-0.6 ± 0.4	-0.6 ± 0.4	-0.6 ± 0.4	-0.6 ± 0.4
Muscle	226MeV	272.0 ± 3.8	-0.5 ± 0.4	-0.4 ± 0.4	-0.5 ± 0.5	-0.4 ± 0.4	-0.4 ± 0.5

Table A.3: The absolute differences between Zebra MLIC D90R measurements and Dual Energy Monoenergetic Plus images calculated D90R related to animal organ samples single spot irradiation are reported.

		Difference from MLIC D90R Measurement: Mean ± STD [mm]				
Tissue	**MLIC D90R Meas. Mean ± STD [mm]**	**Stoich. MONO+ 45keV**	**Stoich. MONO+ 65keV**	**Stoich. MONO+ 70keV**	**Stoich. MONO+ 75keV**	**Stoich. MONO+ 140keV**
Liver	175.0 ± 1.6	0.2 ± 0.3	0.5 ± 0.2	0.5 ± 0.2	0.5 ± 0.2	0.6 ± 0.2
Heart	146.1 ± 5.6	-1.3 ± 1.3	-0.3 ± 1.3	-0.2 ± 1.3	-0.1 ± 1.3	-0.0 ± 1.3
Bone	225.9 ± 4.2	-0.4 ± 0.8	0.5 ± 0.8	0.7 ± 0.8	0.9 ± 0.8	1.1 ± 0.8
Fat	163.2 ± 1.5	1.8 ± 1.1	1.7 ± 1.2	1.7 ± 1.2	1.7 ± 1.2	1.7 ± 1.2
Kydney	163.8 ± 0.6	-1.4 ± 0.4	-0.8 ± 0.4	-0.8 ± 0.4	-0.7 ± 0.4	-0.7 ± 0.4
Muscle	156.5 ± 2.9	0.1 ± 0.7	0.3 ± 0.7	0.4 ± 0.7	0.4 ± 0.7	0.4 ± 0.7

		Difference from MLIC D90R Measurement: Mean ± STD [mm]				
Tissue	**MLIC D90R Meas. Mean ± STD [mm]**	**Stoich. MONO+ 85keV**	**Stoich. MONO+ 90keV**	**Stoich. MONO+ 100keV**	**Stoich. MONO+ 120keV**	**Stoich. MONO+ 140keV**
Liver	175.0 ± 1.6	0.6 ± 0.2	0.6 ± 0.2	0.6 ± 0.2	0.7 ± 0.2	0.7 ± 0.3
Heart	146.1 ± 5.6	0.1 ± 1.3	0.1 ± 1.3	0.1 ± 1.3	0.3 ± 1.4	0.3 ± 1.4
Bone	225.9 ± 4.2	1.2 ± 0.8	1.3 ± 0.8	1.5 ± 0.8	1.8 ± 0.8	1.9 ± 0.9
Fat	163.2 ± 1.5	1.7 ± 1.2	1.7 ± 1.2	1.7 ± 1.2	1.7 ± 1.2	1.7 ± 1.2
Kydney	163.8 ± 0.6	-0.7 ± 0.4	-0.6 ± 0.4	-0.6 ± 0.4	-0.5 ± 0.4	-0.5 ± 0.4
Muscle	156.5 ± 2.9	0.5 ± 0.7	0.5 ± 0.7	0.5 ± 0.7	0.5 ± 0.7	0.5 ± 0.7

Table A.4: The absolute differences between Zebra MLIC D90R measurements and Dual Energy Monoenergetic Plus images calculated D90R related to animal organ samples dose cube irradiation are reported.

Bibliography

[1] Chang JY Liu H. "Proton therapy in clinical practice". In: *Chin J Cancer* (2021). DOI: 10.5732/cjc.010.10529.

[2] Harald Paganetti. "Relative biological effectiveness (RBE) values for proton beam therapy. Variations as a function of biological endpoint, dose, and linear energy transfer". In: *Physics in Medicine Biology* 59.22 (Oct. 2014), R419. DOI: 10.1088/0031-9155/59/22/R419. URL: https://dx.doi.org/10.1088/0031-9155/59/22/R419.

[3] Patrick Wohlfahrt et al. "Clinical Implementation of Dual-energy CT for Proton Treatment Planning on Pseudo-monoenergetic CT scans". In: *International Journal of Radiation Oncology*Biology*Physics* 97.2 (2017), pp. 427–434. ISSN: 0360-3016. DOI: https://doi.org/10.1016/j.ijrobp.2016.10.022. URL: https://www.sciencedirect.com/science/article/pii/S0360301616333429.

[4] Christian Möhler et al. "Experimental verification of stopping-power prediction from single- and dual-energy computed tomography in biological tissues". In: *Physics in Medicine Biology* 63.2 (Jan. 2018), p. 025001. DOI: 10.1088/1361-6560/aaa1c9. URL: https://dx.doi.org/10.1088/1361-6560/aaa1c9.

[5] Patrick Wohlfahrt et al. "Evaluation of Stopping-Power Prediction by Dual- and Single-Energy Computed Tomography in an Anthropomorphic Ground-Truth Phantom". In: *International Journal of Radiation Oncology*Biology*Physics* 100.1 (2018), pp. 244–253. ISSN: 0360-3016. DOI: https://doi.org/10.1016/j.ijrobp.2017.09.025. URL: https://www.sciencedirect.com/science/article/pii/S0360301617338920.

[6] Vicki T. Taasti et al. "A robust empirical parametrization of proton stopping power using dual energy CT". In: *Medical Physics* 43.10 (2016), pp. 5547–5560. DOI: https://doi.org/10.1118/1.4962934. eprint: https://aapm.onlinelibrary.wiley.com/doi/pdf/10.1118/1.4962934. URL: https://aapm.onlinelibrary.wiley.com/doi/abs/10.1118/1.4962934.

[7] Yunhe Xie et al. "Ex vivo validation of a stoichiometric dual energy CT proton stopping power ratio calibration". In: *Physics in Medicine Biology* 63.5 (Mar. 2018), p. 055016. DOI: 10.1088/1361-6560/aaae91. URL: https://dx.doi.org/10.1088/1361-6560/aaae91.

[8] Uwe Schneider, Eros Pedroni, and Antony Lomax. "The calibration of CT Hounsfield units for radiotherapy treatment planning". In: *Physics in Medicine Biology* 41.1 (Jan. 1996), p. 111. DOI: 10.1088/0031-9155/41/1/009. URL: https://dx.doi.org/10.1088/0031-9155/41/1/009.

[9] *Particle therapy facilities in clinical operation*. https://www.ptcog.site/index.php/facilities-in-operation-public. Accessed: 2024-06-24.

[10] Wayne D Newhauser and Rui Zhang. "The physics of proton therapy". In: *Physics in Medicine Biology* 60.8 (Mar. 2015), R155. DOI: 10.1088/0031-9155/60/8/R155. URL: https://dx.doi.org/10.1088/0031-9155/60/8/R155.

[11] Nader Mohamed, Anna Lee, and Nahyun Lee. "Proton beam radiation therapy treatment for head and neck cancer". In: *Precision Radiation Oncology* 6 (Dec. 2021). DOI: 10.1002/pro6.1135.

[12] Dan Jones et al. "ICRU Report No. 78, Prescribing, recording, and reporting proton-beam therapy." In: 2007. URL: https://api.semanticscholar.org/CorpusID:74248405.

[13] Parsons Vitti E. T. "The Radiobiological Effects of Proton Beam Therapy: Impact on DNA Damage and Repair. Cancers". In: *International Journal of Radiation Oncology Biology Physics* (2019). DOI: 10.3390/cancers11070946.

[14] Schreuder AN et al. "Validation of the RayStation Monte Carlo dose calculation algorithm using realistic animal tissue phantoms". In: *Journal of Applied Clinical Medical Physics* (2019). DOI: 10.1002/acm2.12733.

[15] Schultze B et al. "Particle-Tracking Proton Computed Tomography-Data Acquisition, Preprocessing, and Preconditioning". In: *IEEE* (2021). DOI: 10.1109/access.2021.3057760.

[16] Marcel van Herk. "Errors and margins in radiotherapy". In: *Seminars in Radiation Oncology* 14.1 (2004). High-Precision Radiation Therapy of Moving Targets, pp. 52–64. ISSN: 1053-4296. DOI: https://doi.org/10.1053/j.semradonc.2003.10.003. URL: https://www.sciencedirect.com/science/article/pii/S1053429603000845.

[17] F Albertini, E B Hug, and A J Lomax. "Is it necessary to plan with safety margins for actively scanned proton therapy?" In: *Physics in Medicine Biology* 56.14 (June 2011), p. 4399. DOI: 10.1088/0031-9155/56/14/011. URL: https://dx.doi.org/10.1088/0031-9155/56/14/011.

[18] Yang M et al. "Comprehensive analysis of proton range uncertainties related to patient stopping-power-ratio estimation using the stoichiometric calibration". In: *Physics in medicine and biology* (2012). DOI: 10.1088/0031-9155/57/13/4095.

[19] Daphne F. Jackson and D.J. Hawkes. "X-ray attenuation coefficients of elements and mixtures". In: *Physics Reports* 70.3 (1981), pp. 169–233. ISSN: 0370-1573. DOI: https://doi.org/10.1016/0370-1573(81)90014-4. URL: https://www.sciencedirect.com/science/article/pii/0370157381900144.

[20] Cynthia H. McCollough et al. "Principles and applications of multienergy CT: Report of AAPM Task Group 291". In: *Medical Physics* 47.7 (2020), e881–e912. DOI: https://doi.org/10.1002/mp.14157. eprint: https://aapm.onlinelibrary.wiley.com/doi/pdf/10.1002/mp.14157. URL: https://aapm.onlinelibrary.wiley.com/doi/abs/10.1002/mp.14157.

[21] R.A. Rutherford, B.R. Pullan, and I. Isherwood. "Measurement of effective atomic number and electron density using an EMI scanner". In: *Neuroradiology* (1976). DOI: https://doi.org/10.1007/BF00327253.

[22] ICRP. "Report of the Task Group on Reference Man". In: *ICRP Publication 23, Pergamon Press, Oxford* (1975).

[23] Ainsley Christopher G and Caitlyn M Yeager. "Practical considerations in the calibration of CT scanners for proton therapy". In: *Journal of applied clinical medical physics* (2014). DOI: 10.1120/jacmp.v15i3.4721.

[24] Reza Forghani, Bruno De Man, and Rajiv Gupta. "Dual-Energy Computed Tomography: Physical Principles, Approaches to Scanning, Usage, and Implementation: Part 1". In: *Neuroimaging Clinics of North America* 27.3 (2017). Dual Energy CT: Applications in Head and Neck and Neurologic Imaging, pp. 371–384. ISSN: 1052-5149. DOI: https://doi.org/10.1016/j.nic.2017.03.002. URL: https://www.sciencedirect.com/science/article/pii/S1052514917300187.

[25] Antunes C. Curvo-Semedo L. Borges A. P. "Pros and Cons of Dual-Energy CT Systems: "One Does Not Fit All"." In: *Tomography* (2023). DOI: https://doi.org/10.3390/tomography9010017.

[26] R E Alvarez and A Macovski. "Energy-selective reconstructions in X-ray computerised tomography". In: *Physics in Medicine Biology* 21.5 (Sept. 1976), p. 733. DOI: 10.1088/0031-9155/21/5/002. URL: https://dx.doi.org/10.1088/0031-9155/21/5/002.

[27] Joseph R. Grajo and Dushyant V. Sahani. "Dual-Energy CT of the Abdomen and Pelvis: Radiation Dose Considerations". In: *Journal of the American College of Radiology* 15.8 (2018), pp. 1128–1132. ISSN: 1546-1440. DOI: https://doi.org/10.1016/j.jacr.2017.08.012. URL: https://www.sciencedirect.com/science/article/pii/S1546144017310037.

[28] Yeseul Kang et al. "Comparison of image quality, contrast administration, and radiation doses in pediatric abdominal dual-layer detector dual-energy CT using propensity score matching analysis". In: *European Journal of Radiology* 169 (2023), p. 111177. ISSN:

0720-048X. DOI: https://doi.org/10.1016/j.ejrad.2023.111177. URL: https://www.sciencedirect.com/science/article/pii/S0720048X23004916.

[29] Esther Bär et al. "The potential of dual-energy CT to reduce proton beam range uncertainties". In: *Medical Physics* 44.6 (2017), pp. 2332–2344. DOI: https://doi.org/10.1002/mp.12215. eprint: https://aapm.onlinelibrary.wiley.com/doi/pdf/10.1002/mp.12215. URL: https://aapm.onlinelibrary.wiley.com/doi/abs/10.1002/mp.12215.

[30] Magdalena Bazalova et al. "Dual-energy CT-based material extraction for tissue segmentation in Monte Carlo dose calculations". In: *Physics in Medicine Biology* 53.9 (May 2008), p. 2439. DOI: 10.1088/0031-9155/53/9/015. URL: https://dx.doi.org/10.1088/0031-9155/53/9/015.

[31] Joanne K van Abbema et al. "Relative electron density determination using a physics based parameterization of photon interactions in medical DECT". In: *Physics in Medicine Biology* 60.9 (May 2015), p. 3825. DOI: 10.1088/0031-9155/60/9/3825. URL: https://dx.doi.org/10.1088/0031-9155/60/9/3825.

[32] M Yang et al. "Theoretical variance analysis of single- and dual-energy computed tomography methods for calculating proton stopping power ratios of biological tissues". In: *Physics in Medicine Biology* 55.5 (Feb. 2010), p. 1343. DOI: 10.1088/0031-9155/55/5/006. URL: https://dx.doi.org/10.1088/0031-9155/55/5/006.

[33] Alexandra E Bourque, Jean-François Carrier, and Hugo Bouchard. "A stoichiometric calibration method for dual energy computed tomography". In: *Physics in Medicine Biology* 59.8 (May 2014), p. 2059. DOI: 10.1088/0031-9155/59/8/2059. URL: https://dx.doi.org/10.1088/0031-9155/59/8/2059.

[34] Nora Hünemohr et al. "Experimental verification of ion stopping power prediction from dual energy CT data in tissue surrogates". In: *Physics in Medicine Biology* 59.1 (Dec. 2013), p. 83. DOI: 10.1088/0031-9155/59/1/83. URL: https://dx.doi.org/10.1088/0031-9155/59/1/83.

[35] Guillaume Landry et al. "Deriving effective atomic numbers from DECT based on a parameterization of the ratio of high and low linear attenuation coefficients". In: *Physics in Medicine Biology* 58.19 (Sept. 2013), p. 6851. DOI: 10.1088/0031-9155/58/19/6851. URL: https://dx.doi.org/10.1088/0031-9155/58/19/6851.

[36] Arthur Lalonde and Hugo Bouchard. "A general method to derive tissue parameters for Monte Carlo dose calculation with multi-energy CT". In: *Physics in Medicine Biology* 61.22 (Oct. 2016), p. 8044. DOI: 10.1088/0031-9155/61/22/8044. URL: https://dx.doi.org/10.1088/0031-9155/61/22/8044.

[37] David K. Brice. "Stopping powers for electrons and positrons (ICRU report 37; International commission on radiation units and measurements, Bethesda, Maryland, USA, 1984)". In: *Nuclear Instruments & Methods in Physics Research Section B-beam Interactions With Materials and Atoms* 12 (1985), pp. 187–188. URL: https://api.semanticscholar.org/CorpusID:94129151.

[38] David Viar-Hernández et al. "Material decomposition maps based calibration of dual energy CT scanners for proton therapy planning: a phantom study". In: *Physics in Medicine Biology* 69.4 (Feb. 2024), p. 045018. DOI: 10.1088/1361-6560/ad2015. URL: https://dx.doi.org/10.1088/1361-6560/ad2015.

[39] Farace P, Righetto R., and Meijers A. "Pencil beam proton radiography using a multilayer ionization chamber." In: *Physics in Medicine Biology* (2016). DOI: doi:10.1088/0031-9155/61/11/4078.

[40] Thomas Bortfeld. "An analytical approximation of the Bragg curve for therapeutic proton beams". In: *Medical Physics* 24.12 (1997), pp. 2024–2033. DOI: https://doi.org/10.1118/1.598116. eprint: https://aapm.onlinelibrary.wiley.com/doi/pdf/10.1118/1.598116. URL: https://aapm.onlinelibrary.wiley.com/doi/abs/10.1118/1.598116.

[41] Vikren Sarkar et al. "An evaluation of the use of DirectSPR images for proton planning in the RayStation treatment planning software". In: *Journal of Applied Clinical Medical Physics* 24.5 (2023), e13900. DOI: https://doi.org/10.1002/acm2.13900. URL: https://aapm.onlinelibrary.wiley.com/doi/abs/10.1002/acm2.13900.

[42] Manoj Diwakar and Manoj Kumar. "A review on CT image noise and its denoising". In: *Biomedical Signal Processing and Control* 42 (2018), pp. 73–88. ISSN: 1746-8094. DOI: https://doi.org/10.1016/j.bspc.2018.01.010. URL: https://www.sciencedirect.com/science/article/pii/S1746809418300107.

[43] Peters N et al. "Reduction of clinical safety margins in proton therapy enabled by the clinical implementation of dual-energy CT for direct stopping-power prediction." In: *Radiother Oncol* (2022). DOI: 10.1016/j.radonc.2021.11.002.